ACS OMEGA

http://pubs.acs.org/journal/acsodf

Article

# Polymorphs of Titanium Dioxide: An Assessment of the Variants of Projector Augmented Wave Potential of Titanium on Their Geometric and Dielectric Properties

Pradeep R. Varadwaj,* Van An Dinh, Yoshitada Morikawa, and Ryoji Asahi*

Cite This: *ACS Omega* 2023, 8, 22003−22017

Read Online

ACCESS | Metrics & More | Article Recommendations | Supporting Information

**ABSTRACT:** Titanium dioxide ($TiO_2$) is one of the important functional materials owing to its diverse applications in many fields of chemistry, physics, nanoscience, and technology. Hundreds of studies on its physicochemical properties, including its various phases, have been reported experimentally and theoretically, but the controversial nature of relative dielectric permittivity of $TiO_2$ is yet to be understood. Toward this end, this study was undertaken to rationalize the effects of three commonly used projector augmented wave (PAW) potentials on the lattice geometries, phonon vibrations, and dielectric constants of rutile (R-)$TiO_2$ and four of its other phases (anatase, brookite, pyrite, and fluorite). Density functional theory calculations within the PBE and PBEsol levels, as well as their reinforced versions PBE+U and PBEsol+U (U = 3.0 eV), were performed. It was found that PBEsol in combination with the standard PAW potential centered on Ti is adequate to reproduce the experimental lattice parameters, optical phonon modes, and the ionic and electronic contributions of the relative dielectric permittivity of R-$TiO_2$ and four other phases. The origin of failure of the two soft potentials, namely, Ti_pv and Ti_sv, in predicting the correct nature of low-frequency optical phonon modes and ion-clamped dielectric constant of R-$TiO_2$ is discussed. It is shown that the hybrid functionals (HSEsol and HSE06) slightly improve the accuracy of the above characteristics at the cost of a significant increase in computation time. Finally, we have highlighted the influence of external hydrostatic pressure on the R-$TiO_2$ lattice, leading to the manifestation of ferroelectric modes that play a role in the determination of large and strongly pressure-dependent dielectric constant.

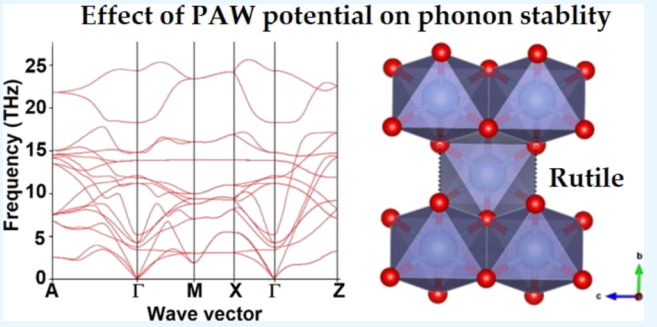


## 1. INTRODUCTION

Semiconducting crystalline $TiO_2$ has been experimentally observed in three different temperature phases.[1−4] These include the rutile phase, the anatase phase, and the brookite phase. The rutile phase, with a band gap of 3.0 eV,[5] exists at temperatures around 1097 and 1172 K and is stable at ambient conditions.[1,2] Allen et al.[6] have found that a mixture of the brookite and anatase phases of $TiO_2$ can be observable up to 772 K, whereas that of the anatase, brookite, and rutile phases can be observable around 872 K, and the rutile-only phase is observable at and above 1097 K. The anatase and brookite phases of $TiO_2$ are semiconducting systems with band gaps of 3.4 eV[7] and 3.3 eV,[8] respectively.

One of the fundamental physical properties of rutile $TiO_2$ (hereafter, R-$TiO_2$) is the relative dielectric permittivity (expressed as $\varepsilon_r$)[9−16] that provides insight into the applicability of Ti-based materials in high energy density storage devices,[17,18] supercapacitors,[19] among other technological areas.[20] A number of theoretical[21−23] and experimental[11−16,24] investigations have been centered on the determination of $\varepsilon_r$. Specifically, Schöche et al.[25] have discussed the low- and high-frequency contributions to $\varepsilon_r$ reported by various authors. From these studies, it is apparent that different research groups have reported different values of $\varepsilon_r$ ($\varepsilon_r$ values between 100 and 10,000). The variability in the observed or proposed values of $\varepsilon_r$ has caused many research attentions owing to the underlying controversy. Bonkerud and co-workers[16] have recently uncovered that the giant $\varepsilon_r$ reported in early studies[11,12] was due to an incorrectly designed experiment or an incorrect interpretation. Their argument was based on the early capacitance measurements that have considered the full thickness of the crystal, where metallic contacts were deposited on opposite sides. In any case, R-$TiO_2$ ceramics when co-doped with Nb + Tr (Tr = Al, In, Ga, Tl, Dy, Gd, La, Y, Sm, V, Li) feature colossal dielectric permittivity.[26−28] The experimental $\varepsilon_r$ values for these systems vary between 10,000 and

Received: March 26, 2023
Accepted: May 24, 2023
Published: June 7, 2023

ACS Publications

© 2023 The Authors. Published by American Chemical Society

100,000. They are yet to be confirmed by first principles and/or density functional theory (DFT) calculations.

Lee et al.[29] have studied the dielectric properties of R-$TiO_2$ using a variety of exchange correlation energy DFT functionals, including the local density approximation (LDA), the LDA+U, the generalized gradient approximation (GGA) method, and the PBE0 and HSE06 hybrid functionals. The essence of the study was that the dielectric properties of R-$TiO_2$ vary upon changing the theoretical methods applied, and the frequencies of phonon vibrations may or may not be softened at high-symmetry points in *k*-space. The $\varepsilon_r$ values calculated using LDA were in close agreement with experiment, and those calculated with the HSE06 functional and LDA+U method were overestimated and severely underestimated, respectively. For instance, the ionic contribution to $\varepsilon_r$ was reported to be 63.7, 40.0, 176.5, 282.1, and 376.4 with LDA+U (U = 3.0 eV), LDA+U (U = 4.36 eV), LDA, PBE0, and HSE06, respectively (see the actual data in Table 1 of ref 29). Our inspection of their data shows that $\varepsilon_r$ is not meaningful with LDA+U and is partially (or significantly) overestimated with the LDA (or PBE0 and HSE06) methods compared to the corresponding experimental mean value of 159.7.[14] Furthermore, the LDA result outlined above was abnormally different from that of 133.5 reported by Shojaee et al.,[23] even though the HSE functional gave a value of 129.3 (exact values 159 and 70 along the $x-y$ plane and $z$-direction, respectively).[30] Interestingly, however, the electronic contribution to $\varepsilon_r$ did not show any strong dependence on the quality of theoretical methods applied (PBE, PBE0, etc.).[21,31−33] The incipient ferroelectric behavior and the low-frequency dielectric constant are directly linked to lattice dynamics, with a strong dependence on the low-frequency transverse optical phonon mode $A_{2u}$.[34,35]

In this study, we have theoretically investigated the lattice properties, zone-center phonon vibrations, and the low- and high-frequency-dependent (ionic and electronic contributions, respectively) dielectric permittivity of rutile (R-)$TiO_2$ using DFT at PBEsol[36] and PBE[37,38] levels, with and without incorporating the Hubbard term U.[39,40] Density functional perturbation theory (DFPT) was employed for the evaluation of phonon vibrations and dielectric properties.[41−43] The same properties were also investigated for the anatase and brookite phases, as well as for the two high-pressure structures of $TiO_2$ (called pyrite[44−46] and fluorite[45−48]) for comparison.

The main objective of our study is to demonstrate the dependency of the above properties on the two DFT functionals employed, as well as that on the three commonly used variants of the projector augmented wave (PAW) potential[49,49,50] available in the Vienna ab initio simulation package (VASP).[51−53] The study is necessary because it is imperative to clarify how and to what extent the promotion of the number of core electrons to valence electrons in the PAW potential(s) affects the accuracy of the physical properties of $TiO_2$ (e.g., lattice geometry, relative permittivity, and phonon frequencies). The two GGA functionals were chosen because PAW potentials are specifically designed for use in conjunction with PBE- and PBE-like functionals (e.g., PBEsol); they are computationally inexpensive and are at the forefront of large-scale, high-throughput calculations for in-silico design of new functional materials. To verify the conclusions arrived at using the two PBE-based functionals, similar calculations for R-$TiO_2$ were performed at a relatively high level using hybrid functionals HSE06[54] and HSEsol.[55] Finally, we have compared our computed results with the low-temperature experimental results.

## 2. COMPUTATIONAL DETAILS

The electronic structure properties of all the five phases of $TiO_2$ were calculated using PBE and PBEsol; the VASP code was used. Hereafter, we refer the anatase-, brookite-, pyrite-, and fluorite phases of $TiO_2$ to as A-, B-, P-, and F-$TiO_2$, respectively.

The PAW potentials were used, in which the core electrons were frozen, and were replaced by pseudopotentials. There are four versions of PAW potential for Ti, distributed by VASP. Depending on the size of the cutoff radius used to define the potential around the nucleus, the PAW potentials have been considered hard or soft, meaning they differ from each other in the degree to which they treat inner-shell electrons as valence electrons. We used three commonly used versions of the PAW potential for Ti, keeping the same for the O site in $TiO_2$ unchanged. We label the standard PAW potential of Ti, which has four valence electrons $3d^3 4s^1$, as Ti_std. The remaining two variants of the PAW potential for Ti are augmented versions, labeled as Ti_pv and Ti_sv, which include $2p^6$ and $2s^2 2p^6$ semi-core states as part of the basis set for valence bands, respectively. The outermost cutoff radii were 2.8, 2.5, and 2.3 Å for Ti_std, Ti_pv, and Ti_sv, respectively. The Wigner−Seitz radii of the corresponding PAW potentials were 1.323, 1.323, and 1.217 Å, respectively.

The crystal lattices of the five phases of $TiO_2$ were fully relaxed without any constraints, starting from their respective experimental structures wherever feasible (see discussion below). The cutoff energy for the plane-wave basis set was set at 520 eV, and the break condition for the electronic relaxation loop was set at $10^{-8}$ eV. The force on each ion was less than 0.002 eV $Å^{-1}$. The *k*-meshes of 9 × 9 × 15, 8 × 8 × 10, 6 × 4 × 6, 10 × 10 × 10, and 8 × 8 × 8 were utilized for R-, A-, B-, F-, and P-$TiO_2$, respectively. High precision, together with a blocked Davidson iteration scheme, was invoked.

The ionic[41,56−58] and electronic (optic)[57−59] contributions ($\varepsilon_{ij}^{(0)}$ and $\varepsilon_{ij}^{(\infty)}$, respectively) to dimensionless total relative dielectric permittivity $\varepsilon_r$ ($\varepsilon_r = \varepsilon_{ij}^{(0)} + \varepsilon_{ij}^{(\infty)}$) were calculated at the same levels of theory (PBE and PBEsol) for all the three PAW potentials mentioned above. DFPT was employed since it provides better estimation of the relative dielectric permittivity at the expense of computational time, especially when compared with experiment. The finite difference method (FDM)[60−62] is computationally expensive, which was also considered in conjunction with the hybrid functionals and GGA to examine whether $\varepsilon_r$ obtained with this method are comparable with those emerged from DFPT/GGA. The same *k*-meshes used for the convergence of crystal lattices and evaluation of other properties were used for the calculation of $\varepsilon_{ij}^{(0)}$. The cutoff energy was set at 520, 600, and 700 eV that enabled us to test the dependence of the cutoff energy for plane-wave on $\varepsilon_{ij}^{(0)}$ and $\varepsilon_{ij}^{(\infty)}$ and $\varepsilon_r$.

For reasons discussed in the following section, the hybrid functionals, HSE06 and HSEsol, were employed to obtain the relaxed lattice geometry, phonon modes, and dielectric permittivity of R-$TiO_2$. A 4 × 4 × 6 *k*-mesh was chosen both for geometry relaxation and phonon mode analysis. The cutoff energy for the plane-wave basis set, the total energy convergence for electronic relaxation, and the residual forces used for ionic relaxation were 520 eV, $10^{-6}$ eV, and 0.002 eV $Å^{-1}$, respectively. The FDM was applied for the calculation of


https://doi.org/10.1021/acsomega.3c02038
ACS Omega 2023, 8, 22003−22017

the phonon vibrational modes and relative dielectric permittivity. The cutoff energy for the plane-wave basis set and the ion relaxation loop were 600 and $10^{-6}$ eV, respectively.

Phonon dispersion and Raman spectra were calculated using FDM.[63,64] The PBEsol relaxation geometries of R-$TiO_2$, A-$TiO_2$, and B-$TiO_2$ were used to construct supercells consisting of 72, 108, and 96 atoms, respectively. A 3 × 3 × 3 *k*-mesh was used to calculate phonon dispersion for all three systems above. For the calculation of the Raman spectra, the size of the *k*-mesh was chosen to be 9 × 9 × 15, 8 × 8 × 4, and 6 × 6 × 4 for the corresponding systems, respectively. The cutoff energy was set to 520 eV, and the energy for electronic relaxation loop and the residual force were converged to within $10^{-7}$ eV and 0.02 eV $Å^{-1}$, respectively. For cubic P- and F-$TiO_2$, supercells with cell sizes close to 10 Å were used, consisting of 96 and 192 atoms, respectively. A *k*-mesh of 2 × 2 × 2 was used, together with the electronic relaxation loop and the residual force that were set converged to within $10^{-8}$ eV and 0.02 eV $Å^{-1}$, respectively. The DFPT formalism was utilized, together with the Phonopy code.[65]

## 3. RESULTS AND DISCUSSION

**3.1. Lattice Properties.** The fully relaxed lattice geometries of all the five phases of $TiO_2$ are shown in Figure 1.

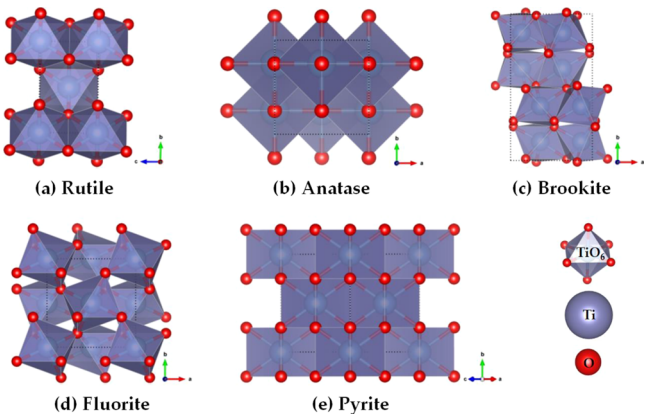


**Figure 1.** (a)−(e) Polyhedral models of the PBEsol relaxed unit-cell geometries of the five phases of $TiO_2$, obtained with Ti_std. The orientation of the crystallographic axes *a*, *b*, and *c* is shown for each case.

Tables 123 list the calculated lattice properties of R-, A-, and B-phases of $TiO_2$ and compare them with experiment. The properties include the lattice constants (*a*, *b*, *c*, *α*, *β*, and *γ*), cell volume *V*, and mass density *ρ*.

Experimental lattice constants ~~even~~ reported for the three major phases of $TiO_2$ vary widely from one research group to another.[56,66−72] The variation may be due to the differences in the experimental conditions and the fitting methods adopted in measuring and refining the structural data. A similar attribute is notable of the data obtained using two DFT functionals and the three variants of the PAW potential, as well as when the Hubbard U (U = 3.0 eV) term was combined with GGA.

From Table 1, it may be seen that the lattice constants of R-$TiO_2$ follow the trend: $a = b \neq c$ and $\alpha = \beta = \gamma = 90°$. PBEsol reproduces lattice constants and cell volumes, which are in fair agreement with the experimental range of reported values (not shown). In contrast, the PBE functional systematically overestimates the same properties (Table 1). The same is also observed when both of them were compared with ~~to~~ the high-precision experimental data reported so far with an *R*-factor (discrepancy index) as low as 1.47%.[66] For a particular GGA method, PBE or PBEsol, when passed from Ti_std via Ti_pv to Ti_sv, the lattice constants ($a = b$ and $c$) and cell volume were systematically decreased; this is opposite to the trend in the mass density that was increased. The result suggests that the lattice constant or cell volume tends to decrease and mass density tends to increase as the PAW potential softens. Conversely, the HSE06 method gave improved lattice properties over HSEsol. The main difference between PBEsol and HSE lies in the lattice volume, in which the predictability of the former is relatively accurate compared to that feasible in the crystal.

The DFT-U method did not show any dramatic improvement in the lattice properties. Rather, it significantly overestimates all the lattice constants, with a consequent increase in the cell volume. The reducing behavior of the lattice constants observed with DFT was observed with DFT+U when passing from Ti_std via Ti_pv to Ti_sv.

A-$TiO_2$ is metastable. It is stable only up to a temperature of 600 °C. Beyond this temperature, a transformation to rutile phase occurs, even though the reported thermal analysis suggests that the transformation from anatase to rutile may start at a temperature of around 400 °C.[73] The geometry of A-$TiO_2$ is tetragonal, with space group $I4_1/amd$ (*141*), and the unit and primitive cells contain four and two formula units of $TiO_2$, respectively. Table 2 summarizes the conventional unit-cell lattice properties of A-$TiO_2$, obtained from this work and reported experimentally. Since PBEsol-calculated lattice properties agree well with experiment for R-$TiO_2$ (cf. Table 1), we did not consider the PBE and DFT+U methods to compute the lattice properties for A-$TiO_2$. Table 2 summarizes the PBEsol results that demonstrate that Ti_std slightly overestimates the lattice constants and cell volume and underestimates the mass density compared to experiment.[68] There is no appreciable improvement in these properties upon increasing the size of the PAW potential from Ti_std through Ti_pv to Ti_sv. PBEsol+U has overestimated the lattice constants and cell volume and underestimated the mass density, all compared to experiment.

The crystal structure of B-$TiO_2$ is orthorhombic. It has eight formula units of $TiO_2$ (space group *Pbca* (*61*)). Several experimental studies have reported the crystal structure of B-$TiO_2$, showing a dispersion in the values of the lattice properties. For instance, Murugesan et al.[68] (Silva Junior et al.[74]) [Nishio-Hamane et al.[75]] {Rezaee et al.[70]} have reported $a$ = 5.144 Å (5.138; 5.259) [4.596] {4.492}, $b$ = 9.293 (9.194; 9.202) [8.962] {9.101} Å, and $c$ = 5.412 (5.449; 5.47) [4.823] {5.455} Å. Because of the variation in the lattice constants, the nature of both *V* and *ρ* is changed appreciably. The *V* values extracted from the unit cells of the corresponding crystals were 258.711 (256.844; 264.711) [198.656] {245.341} $Å^3$. Our PBEsol results are very close to those reported by Murugesan et al.[68] (Table 3). There is a monotonic decrease in the lattice constants with respect to the increase in the number of core electrons as valence electrons in the PAW potentials, an observation which is very similar to that found for R- and A-$TiO_2$ (vide supra).

Table 4 summarizes the calculated lattice properties of P- and F-phases of $TiO_2$. These are compared with the properties of corresponding crystals deposited to the Materials Project database[76] (IDs: mp-1102591[77] and mp-1008677,[78] respec-


https://doi.org/10.1021/acsomega.3c02038
ACS Omega 2023, 8, 22003−22017

Table 1. Comparison of PBE, PBEsol, PBE+U, and PBEsol+U Computed Lattice Constants ($a = b \neq c$ and $\alpha = \beta = \gamma$), Cell Volume ($V$), and Mass Density ($\rho$) of R-$TiO_2$ with Experiment[a,b]

| PAW | $a = b$/Å | $c$/Å | $V$/Å$^3$ | $\rho$/gcm$^{-3}$ | $a = b$/Å | $c$/Å | $V$/Å$^3$ | $\rho$/gcm$^{-3}$ |
|---|---|---|---|---|---|---|---|---|
| | PBE | | | | PBE+U | | | |
| Ti_std | 4.661 | 2.970 | 64.52 | 4.11 | 4.687 | 3.023 | 66.41 | 3.99 |
| Ti_pv | 4.652 | 2.968 | 64.23 | 4.13 | 4.673 | 3.014 | 65.82 | 4.03 |
| Ti_sv | 4.645 | 2.969 | 64.05 | 4.14 | 4.665 | 3.007 | 65.42 | 4.05 |
| | PBEsol | | | | PBEsol+U | | | |
| Ti_std | 4.615 | 2.949 | 62.79 | 4.22 | 4.640 | 3.000 | 64.59 | 4.11 |
| Ti_pv | 4.600 | 2.943 | 62.28 | 4.26 | 4.623 | 2.989 | 63.89 | 4.15 |
| Ti_sv | 4.596 | 2.941 | 62.12 | 4.27 | 4.614 | 2.982 | 63.49 | 4.18 |
| | HSEsol | | | | | | | |
| Ti_std | 4.572 | 2.934 | 61.33 | 4.32 | | | | |
| Ti_pv | 4.556 | 2.934 | 60.91 | 4.36 | | | | |
| Ti_sv | 4.551 | 2.931 | 60.70 | 4.37 | | | | |
| | HSE06 | | | | | | | |
| Ti_std | 4.603 | 2.947 | 62.43 | 4.25 | | | | |
| Ti_pv | 4.590 | 2.949 | 62.13 | 4.27 | | | | |
| Ti_sv | 4.584 | 2.947 | 61.92 | 4.28 | | | | |
| expt.[66] | 4.601 | 2.964 | 62.745 | 4.23 | 4.601 | 2.964 | 62.745 | 4.23 |

[a]$\alpha = \beta = \gamma = 90°$ for the theoretical methods applied. [b]Three different PAW potentials used.

Table 2. Comparison of PBEsol and PBEsol+U Level Lattice Constants ($a = b \neq c$ and $\alpha = \beta = \gamma$), Cell Volume ($V$), and Mass Density ($\rho$) of A-$TiO_2$ with Experiment[a,b]

| | PBEsol | | | | | PBEsol+U | | | | |
|---|---|---|---|---|---|---|---|---|---|---|
| PAW | $a$/Å | $b$/Å | $c$/Å | $V$/Å$^3$ | $\rho$/gcm$^{-3}$ | $a$/Å | $b$/Å | $c$/Å | $V$/Å$^3$ | $\rho$/gcm$^{-3}$ |
| Ti_std | 3.800 | 3.800 | 9.547 | 137.85 | 3.85 | 3.858 | 3.858 | 9.553 | 142.19 | 3.73 |
| Ti_pv | 3.777 | 3.777 | 9.575 | 136.59 | 3.88 | 3.827 | 3.827 | 9.591 | 140.47 | 3.78 |
| Ti_sv | 3.773 | 3.773 | 9.564 | 136.14 | 3.90 | 3.817 | 3.817 | 9.575 | 139.49 | 3.80 |
| expt.[68] | 3.784 | 3.784 | 9.518 | 136.28 | 3.89 | 3.784 | 3.784 | 9.518 | 136.28 | 3.89 |

[a]$\alpha = \beta = \gamma = 90°$ for the theoretical methods applied. [b]Three different PAW potentials used.

Table 3. Comparison of PBEsol and PBEsol+U Level Lattice Constants ($a = b \neq c$ and $\alpha = \beta = \gamma$), Cell Volume ($V$), and Mass Density ($\rho$) of B-$TiO_2$ with Experiment[a,b]

| | PBEsol | | | | | PBEsol+U | | | | |
|---|---|---|---|---|---|---|---|---|---|---|
| PAW | $a$/Å | $b$/Å | $c$/Å | V/Å$^3$ | $\rho$/gcm$^{-3}$ | $a$/Å | $b$/Å | $c$/Å | V/Å$^3$ | $\rho$/gcm$^{-3}$ |
| Ti_std | 5.149 | 9.203 | 5.463 | 258.88 | 4.10 | 5.228 | 9.262 | 5.519 | 267.22 | 3.97 |
| Ti_pv | 5.127 | 9.186 | 5.449 | 256.64 | 4.13 | 5.203 | 9.243 | 5.489 | 263.94 | 4.02 |
| Ti_sv | 5.124 | 9.177 | 5.444 | 255.95 | 4.15 | 5.190 | 9.227 | 5.476 | 262.23 | 4.05 |
| expt.[68] | 5.144 | 9.293 | 5.412 | 258.71 | 4.10 | 5.144 | 9.293 | 5.412 | 258.71 | 4.10 |
| expt.[69] | 5.137 | 9.714 | 5.452 | 256.94 | 4.13 | 5.137 | 9.714 | 5.452 | 256.94 | 4.13 |
| expt.[70] | 4.981 | 9.082 | 5.53 | 250.14 | 4.24 | 4.981 | 9.082 | 5.53 | 250.14 | 4.24 |

[a]$\alpha = \beta = \gamma = 90°$ for the theoretical methods applied. [b]Three different PAW potentials used.

tively), as a result of the lack of experimentally known data. In any case, the PBEsol lattice constants are all slightly underestimated relative to the PBE, with a concomitant decrease in the cell volume and an increase of mass density. The trend in the cell properties for a given correlated method with respect to the three PAW potentials is consistent with that observed for R-, A-, and B-$TiO_2$ (see above). We have observed that F- and P-$TiO_2$ lattices are relatively denser than that of the brookite, anatase, and rutile lattices of $TiO_2$, in agreement with the computational data of Dharmale et al.[44]

### 3.2. Phonon Vibrations and Dynamical Stability.

Born's stability criterion[79,80] suggests that a crystal lattice is said to be dynamically stable if the normal mode vibration frequencies of all the optical phonons are positive, that is, if the eigenvalues of the dynamical matrix are all positive. To this end, we investigated the nature of phonon vibrational frequencies for all the five phases of $TiO_2$, in combination with three PAW potentials. The frequencies of IR- and Raman-active modes of R- and A-$TiO_2$ are summarized in Tables 5 and 6, respectively, whereas those of B-$TiO_2$ are summarized in Table S1; the PBE and experimental phonon frequencies are included in these tables wherever applicable.

Figures 234 show the phonon dispersion curves of R-, A-, and B-$TiO_2$, respectively. Figure 5a,b illustrates the same curves for F- and P-$TiO_2$, respectively. For the first three cases, the phonon modes are all stable at the center of the zone, $\Gamma(k$ (0,0,0)), and at other points of high symmetry along the direction of the wave vector of the first Brillouin zone. That is, the optical phonon modes do not involve any imaginary frequencies, confirming that the R-, A-, and B-$TiO_2$ lattices are dynamically stable irrespective of the three PAW potentials utilized.



https://doi.org/10.1021/acsomega.3c02038
ACS Omega 2023, 8, 22003−22017

Table 4. Comparison of Lattice Constants ($a = b = c$ and $\alpha = \beta = \gamma$), Cell Volume ($V$), and Mass Density ($\rho$) of P- and F-$TiO_2$, Obtained Using PBEsol and PBE, with Those Catalogued in the Materials Project Database (Calculated with [PBE/Ti_pv][76])[a]

| PAW | PBEsol | | | PBE | | |
|---|---|---|---|---|---|---|
| | $a = b = c$ | $V$/Å$^3$ | $\rho$/gcm$^{-3}$ | $a = b = c$ | $V$/Å$^3$ | $\rho$/gcm$^{-3}$ |
| | | | Pyrite (Cubic, $P\text{-}a\bar{3}$) | | | |
| Ti_std | 4.861 | 114.84 | 4.62 | 4.905 | 118.03 | 4.49 |
| Ti_pv | 4.852 | 114.22 | 4.64 | 4.902 | 117.78 | 4.50 |
| Ti_sv | 4.848 | 113.97 | 4.65 | 4.899 | 117.55 | 4.51 |
| mp-1102591[77] | 4.902 | 117.79 | 4.50 | 4.902 | 117.79 | 4.50 |
| | | | Fluorite (Cubic, $Fm\text{-}\bar{3}m$) | | | |
| Ti_std | 4.789 | 109.87 | 4.83 | 4.836 | 113.12 | 4.69 |
| Ti_pv | 4.786 | 109.63 | 4.84 | 4.838 | 113.25 | 4.68 |
| Ti_sv | 4.783 | 109.40 | 4.85 | 4.835 | 113.05 | 4.69 |
| mp-1008677[78] | 4.84 | 113.38 | 4.68 | 4.840 | 113.38 | 4.68 |

[a]Three different PAW potentials used.

Table 5. Comparison of Zone-Center Fundamental IR and Raman Phonon Frequencies $\omega$ (cm$^{-1}$), as Well as IR Intensities $I$ (km/mol) of Rutile-$TiO_2$, Obtained Using PBEsol and PBE Functionals, in Conjunction with the PAW Potentials Ti_std, Ti_pv, and Ti_sv Centered on Ti[abcdef]

| | | | PBEsol | | | | | | PBE | | | | | |
|---|---|---|---|---|---|---|---|---|---|---|---|---|---|---|
| | | | Ti_std | | Ti_pv | | Ti_sv | | Ti_std | | Ti_pv | | Ti_sv | |
| symmetry[f] | expt[g] | expt[h,i] | $\omega$ | $I$ | Ω | $I$ | $\omega$ | $I$ | $\omega$ | $I$ | $\omega$ | $I$ | $\omega$ | $I$ |
| $B_{2g}$(R) | 825.5 | 826 (826.6) | 810.2 | 0.0 | 795.3 | 0.0 | 793.1 | 0.0 | 783.6 | 0.0 | 770.3 | 0.0 | 769.3 | 0.0 |
| $A_{1g}$(R) | 609.8 | 612 (610.4) | 605.8 | 0.0 | 591.0 | 0.0 | 589.8 | 0.0 | 580.9 | 0.0 | 568.4 | 0.0 | 568.0 | 0.0 |
| $E_u$(IR) | | 500 (494.0) | 495.3 | 20.7 | 476.9 | 13.4 | 478.4 | 13.2 | 481.8 | 15.3 | 467.8 | 10.5 | 468.9 | 10.3 |
| $E_u$(IR) | | 500 (494.0) | 495.3 | 20.7 | 476.9 | 13.4 | 478.3 | 13.2 | 481.8 | 15.3 | 467.8 | 10.5 | 468.9 | 10.3 |
| $E_g$(R) | 445.8 | 447 (444.9) | 459.6 | 0.0 | 448.0 | 0.0 | 447.1 | 0.0 | 440.6 | 0.0 | 430.0 | 0.0 | 429.6 | 0.0 |
| $E_g$(R) | 445.8 | 447 (444.9) | 459.6 | 0.0 | 448.0 | 0.0 | 447.1 | 0.0 | 440.6 | 0.0 | 430.0 | 0.0 | 429.6 | 0.0 |
| $A_{2g}$ (S) | | | 405.5 | 0.0 | 413.6 | 0.0 | 415.1 | 0.0 | 407.7 | 0.0 | 414.8 | 0.0 | 416.4 | 0.0 |
| $B_{1u}$(S) | | (406.3) | 395.8 | 0.0 | 372.5 | 0.0 | 373.9 | 0.0 | 369.7 | 0.0 | 354.3 | 0.0 | 357.1 | 0.0 |
| $E_u$(IR) | | 388 (374.4) | 375.0 | 9.7 | 366.4 | 4.0 | 366.9 | 3.7 | 356.9 | 3.2 | 353.9 | 1.0 | 355.1 | 0.9 |
| $E_u$(IR) | | 388 (374.7) | 375.0 | 9.7 | 366.4 | 4.0 | 366.9 | 3.7 | 356.9 | 3.2 | 353.9 | 1.0 | 355.0 | 0.9 |
| $A_{2u}$(IR) | | 167 (188.8) | 180.5 | 179.2 | 61.2 | 168.0 | 71.2 | 165.3 | 99.6 | 184.2 | 106.1$i$ | 171.5 | 98.8$i$ | 168.3 |
| $E_u$(IR) | 235.5 | 183 (172.7) | 158.7 | 105.2 | 93.0 | 110.1 | 98.4 | 108.5 | 95.4 | 115.5 | 62.8 $i$ | 114.1 | 54.3$i$ | 111.5 |
| $E_u$(IR) | 235.5 | 183 (172.7) | 158.7 | 105.2 | 93.0 | 110.1 | 98.2 | 108.4 | 95.4 | 115.5 | 62.8 $i$ | 114.1 | 54.5$i$ | 111.7 |
| $B_{1g}$(R) | 140.2 | 143 (141.6) | 134.2 | 0.0 | 139.7 | 0.0 | 140.5 | 0.0 | 143.9 | 0.0 | 148.5 | 0.0 | 149.0 | 0.0 |
| $B_{1u}$(S) | | (113.0) | 118.3 | 0.0 | 74.9 | 0.0 | 78.3 | 0.0 | 84.8 | 0.0 | 30.1$i$ | 0.0 | 16.7$i$ | 0.0 |
| $A_{2u}$(IR) | | | 0.0 | 13.7 | 0.1 | 8.5 | 0.4 | 8.2 | 0.0 | 8.9 | 0.1 | 8.3 | 0.6 | 9.0 |
| $E_u$(IR) | | | 0.0 | 9.1 | 0.1 | 8.5 | 0.3 | 8.3 | 0.0 | 8.9 | 0.1 | 8.3 | 0.4 | 11.6 |
| $E_u$(IR) | | | 0.0 | 9.1 | 0.1 | 13.0 | 0.2 | 12.6 | 0.1 | 14.2 | 0.1 | 13.2 | 0.4 | 10.1 |

[a]Experimental frequencies are included wherever available, and an energy cutoff of 700 eV was used. [b]Negative value in columns 12 and 14 represent imaginary frequency. [c]Schöche et al.[25] reported the four room-temperature IR-active phonon modes (three degenerate $E_u$ and one non-degenerate $A_{2u}$) to be 188.6 ± 1.2, 379.3 ± 0.2, 500.5 ± 0.3, and 172.3 ± 1.9 cm$^{-1}$, respectively. [d]Gervais and Piriou[85] reported the four IR-active phonon modes (three degenerate $E_u$ and one non-degenerate $A_{2u}$) at 189, 381.5, 508, and 172 cm$^{-1}$, respectively. [e]Eagles reported the four IR-active phonon modes (three degenerate $E_u$ and one non-degenerate $A_{2u}$) at 183, 388, 500, and 167 cm$^{-1}$, respectively.[86] [f]R, IR, and S correspond to Raman- and IR-active and silent modes, respectively. [g]Ref 83. [h]Ref 82. [i]Values in parentheses represent coherent inelastic neutron determination of phonon frequencies at high-symmetry points of Brillouin zone.[81]

For F-$TiO_2$, the optical phonons are unstable along the path Γ−L−W−X, even though they are stable at the Γ-point (Figure 5a). For P-$TiO_2$, several low-frequency phonon modes are unstable throughout the Brillouin zone including zone center. The instability of the phonon modes is understood owing to their (negative) imaginary frequencies (Figure 5b). The result is not perplexed for pressure-driven crystal lattices, as are commonly observed to be dynamically unstable.

The rutile phase of $TiO_2$ has 15 optical phonon modes. Of these, three are acoustic phonon modes. At Γ($k$ (0,0,0)), the optical phonons are representation given by $1A_{1g} + 1A_{2g} + 1A_{2u} + 1B_{1g} + 2B_{1u} + 1B_{2g} + 1E_g + 3\ E_u$, in which $E_g$ (non-polar), $B_{2g}$, $B_{1g}$, and $A_{1g}$ are Raman-active and the $A_{2g}$ (non-polar) and $B_{1u}$ modes are infrared (IR) and Raman inactive silent modes.[81] Each phonon mode $E$ is twofold degenerate, and the phonon modes $A_{2u}$ and $E_u$ are polar.

The four experimentally determined Raman-active modes of R-$TiO_2$ appear at frequencies $\omega$ of 143 ($B_{1g}$), 447 ($E_g$), 612 ($A_{1g}$), and 826 cm$^{-1}$ ($B_{2g}$).[81,82] The corresponding frequencies measured by Ma et al.[83] center at 140.2, 445.8, 609.8, and 825.5 cm$^{-1}$, respectively. They have also measured a broad and moderately strong band that peaks at 235 cm$^{-1}$. This mode is composed of high-level anharmonicity and arises from two-


https://doi.org/10.1021/acsomega.3c02038
ACS Omega 2023, 8, 22003−22017

Table 6. Comparison of Fundamental IR and Raman Frequencies $\omega$ ($cm^{-1}$), as Well as IR Intensities $I$ (km/mol), Obtained Using PBEsol and PBE Functionals, in Conjunction with PAW Potentials Ti_std, Ti_pv, and Ti_sv Centered on Ti of A-$TiO_2$[a,b]

| | | PBEsol | | | | | | PBE | | | | | |
|---|---|---|---|---|---|---|---|---|---|---|---|---|---|
| | | Ti_std | | Ti_pv | | Ti_sv | | Ti_std | | Ti_pv | | Ti_sv | |
| | expt[c,d] | $\omega$ | $I$ | $\omega$ | $I$ | $\omega$ | $I$ | $\omega$ | $I$ | $\omega$ | $I$ | $\omega$ | $I$ |
| $E_g$(R) | 640 (632.7) | 640.4 | 0.0 | 619.8 | 0.0 | 620.6 | 0.0 | 616.5 | 0.0 | 599.7 | 0.0 | 599.7 | 0.0 |
| $E_g$(R) | 640 (632.7) | 640.4 | 0.0 | 619.8 | 0.0 | 620.6 | 0.0 | 616.5 | 0.0 | 599.7 | 0.0 | 599.7 | 0.0 |
| $B_{2u}$ (S) | | 548.6 | 0.0 | 535.9 | 0.0 | 534.4 | 0.0 | 531.0 | 0.0 | 519.2 | 0.0 | 518.6 | 0.0 |
| $A_{1g}$(R) | 519 (515.4) | 516.7 | 0.0 | 510.8 | 0.0 | 510.7 | 0.0 | 499.6 | 0.0 | 493.9 | 0.0 | 494.4 | 0.0 |
| $B_{1g}$(R) | 515 (515.4) | 497.5 | 0.0 | 487.3 | 0.0 | 489.0 | 0.0 | 478.5 | 0.0 | 475.1 | 0.0 | 477.6 | 0.0 |
| $E_u$(IR) | 435 (TO) | 446.0 | 76.7 | 419.0 | 51.1 | 420.7 | 50.1 | 412.0 | 57.9 | 395.3 | 34.6 | 396.5 | 32.8 |
| $E_u$(IR) | 435 (TO) | 446.0 | 76.7 | 419.0 | 51.1 | 420.7 | 50.1 | 412.0 | 57.9 | 395.3 | 34.6 | 396.5 | 32.8 |
| $B_{1g}$(R) | 400 (396.0) | 385.4 | 0.0 | 374.2 | 0.0 | 374.1 | 0.0 | 374.9 | 0.0 | 361.7 | 0.0 | 361.8 | 0.0 |
| $A_{2u}$(IR) | 366 (LO) | 355.9 | 100.3 | 326.6 | 93.3 | 326.9 | 92.0 | 323.3 | 101.5 | 300.0 | 94.0 | 301.2 | 92.8 |
| $E_u$(IR) | 262 (TO) | 240.8 | 75.4 | 227.6 | 90.5 | 231.5 | 89.2 | 226.3 | 95.8 | 209.0 | 107.9 | 211.0 | 106.9 |
| $E_u$(IR) | 262 (TO) | 240.8 | 75.4 | 227.6 | 90.5 | 231.3 | 89.2 | 226.3 | 95.8 | 209.0 | 107.9 | 211.0 | 107.0 |
| $E_g$(R) | 197 (196.3) | 164.7 | 0.0 | 167.1 | 0.0 | 169.2 | 0.0 | 168.4 | 0.0 | 173.4 | 0.0 | 175.9 | 0.0 |
| $E_g$(R) | 197 (196.3) | 164.7 | 0.0 | 167.1 | 0.0 | 169.2 | 0.0 | 168.3 | 0.0 | 173.4 | 0.0 | 175.9 | 0.0 |
| $E_g$(R) | 144 (140.9) | 151.4 | 0.0 | 135.2 | 0.0 | 137.9 | 0.0 | 130.7 | 0.0 | 113.9 | 0.0 | 115.2 | 0.0 |
| $E_g$(R) | 144 (140.9) | 151.3 | 0.0 | 135.2 | 0.0 | 137.6 | 0.0 | 130.7 | 0.0 | 113.9 | 0.0 | 115.1 | 0.0 |
| $A_{2u}$(IR) | | 0.0 | 8.2 | 0.0 | 9.4 | 0.0 | 7.1 | 0.0 | 10.1 | 0.0 | 7.2 | 0.0 | 9.1 |
| $E_u$(IR) | | 0.0 | 9.9 | 0.0 | 9.3 | 0.1 | 9.2 | 0.0 | 9.8 | 0.0 | 9.4 | 0.0 | 7.2 |
| $E_u$(IR) | | 0.0 | 9.6 | 0.0 | 7.2 | 0.2 | 9.2 | 0.0 | 8.1 | 0.0 | 9.4 | 0.1 | 9.3 |

[a]IR, R, and S represent IR-active, Raman-active, and silent modes, respectively. [b]Raman-active modes reported by Arsov et al. were 144 ($E_g$), 197 ($E_g$), 399 ($B_{1g}$), 516 ($A_{1g}$), 516 ($B_{1g}$), and 639 ($E_g$) $cm^{-1}$.[82] [c]IR-active and Raman-active modes are from refs 92 and 93, respectively. [d]Ref 83.

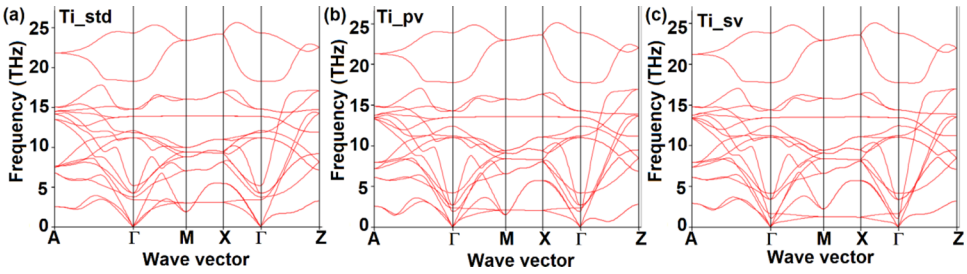


**Figure 2.** Phonon dispersion of R-$TiO_2$, obtained using DFPT in combination with PBEsol and the three PAW potentials centered at the Ti site of the crystal lattice: (a) Ti_std; (b) Ti_pv; and (c) Ti_sv. The phonon frequencies in the vertical axis are in THz (1 THz = 33.3564 $cm^{-1}$).

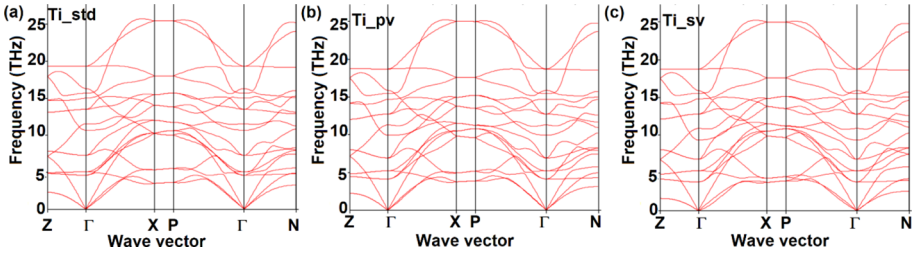


**Figure 3.** Phonon band structure of A-$TiO_2$, obtained using DFPT in combination with PBEsol and the three variants of the PAW potential centered at the Ti site of the crystal lattice: (a) Ti_std; (b) Ti_pv; and (c) Ti_sv. The phonon frequencies in the vertical axis are in THz (1 THz = 33.3564 $cm^{-1}$).

phonon scattering. The same feature was observed by Tompsett et al.[84]

The frequencies of the four vibrational bands observed by Ma et al.[83] and others[81,82] (see above) are in close match with our results (all within 15 $cm^{-1}$). For instance, they are centered at frequencies of 134.2 ($B_{1g}$), 459.6 ($E_g$), 605.8 ($A_{1g}$), and 810.2 $cm^{-1}$ ($B_{2g}$) with [PBEsol/Ti_std], respectively. When Ti_pv and Ti_sv were used, the two high-frequency modes, $A_{1g}$ and $B_{2g}$, could be appreciably underestimated, except for the low-frequency phonon modes, $B_{1g}$ and $E_g$. This comparison leads to a conclusion that the overall nature of the phonon modes reported using coherent inelastic neutron scattering measurements[81] matches well with those computed with Ti_std. The PBEsol frequency of the lowest (silent) phonon mode calculated using Ti_std ($\omega$ = 118.3 $cm^{-1}$) is largely overestimated relative to that obtained using Ti_pv and Ti_sv ($\omega$ = 74.9 and 78.3 $cm^{-1}$, respectively). The latter two are


https://doi.org/10.1021/acsomega.3c02038
ACS Omega 2023, 8, 22003−22017

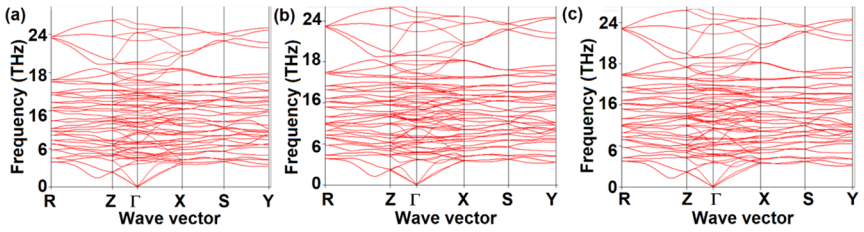


**Figure 4.** Phonon band structure of B-$TiO_2$, obtained using DFPT in combination with PBEsol and the three variants of the PAW potential centered at the Ti site of the crystal lattice: (a) Ti_std; (b) Ti_pv; and (c) Ti_sv. The phonon frequencies in the vertical axis are in THz (1 THz = 33.3564 $cm^{-1}$).

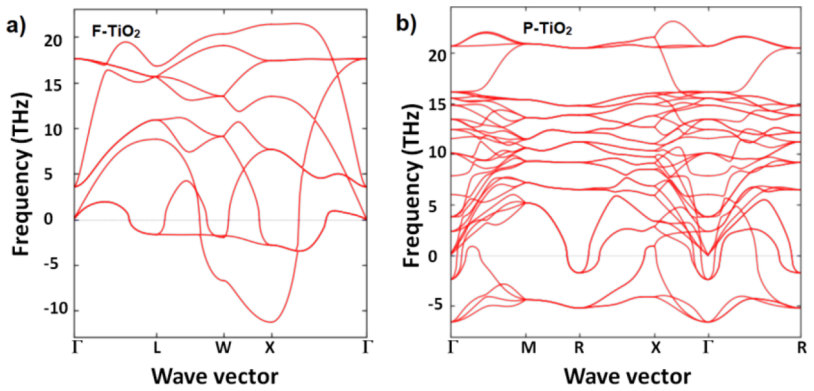


**Figure 5.** (a,b) Illustration of phonon dispersion of F- and P-$TiO_2$, respectively, obtained using DFPT at the [PBEsol/Ti_std] level. The 4 × 4 × 4 (192 atoms) and 2 × 2 × 2 (96 atoms) supercells were utilized for the phonon calculations for F- and P-$TiO_2$, respectively. Phonon frequencies in the vertical axis are in THz (1 THz = 33.3564 $cm^{-1}$).

unquestionably underestimated by 38.1 and 34.7 $cm^{-1}$ compared to experiment ($\omega$ = 113.0 $cm^{-1}$, see Table 5).

R-$TiO_2$ has four IR-active optical phonon modes. Schöche et al.[25] have found that the IR-active modes (three $E_u$ and one $A_{2u}$) possess phonon frequencies of 188.6 ± 1.2, 379.3 ± 0.2, 500.5 ± 0.3, and 172.3 ± 1.9 $cm^{-1}$, respectively. The first three are doubly degenerate modes and the latter one is a non-degenerate mode. Gervais and Piriou[85] [Eagles[86]] have reported that the corresponding phonon mode frequencies should show at frequencies of 189 [183], 381.5 [388], 508 [500], and 172 [167] $cm^{-1}$, respectively. The IR-active modes reported in different studies are not in disagreement with each other. However, the inelastic neutron scattering study did not observe the degenerate vibrational mode at 381.5 $cm^{-1}$, assigned by Gervais and Piriou.[85] Schöche et al.[25] have assigned the two $E_u$ modes to have frequencies of 188.61 and 365.74 $cm^{-1}$, which are the first transverse optical (TO) and longitudinal optical (LO) modes, respectively.

Indeed, the experimental IR phonon modes are consistent with our PBEsol-based frequencies summarized in Table 5. This functional, together with Ti_std, has underestimated the lowest IR-active mode at 158.7 $cm^{-1}$, compared to the experimental value of 183 (172.7) $cm^{-1}$. Ti_pv and Ti_sv underestimated them further to appear at frequencies of 93.0 and 98.3 $cm^{-1}$, respectively. Interestingly, Ti_sv has predicted the frequencies of the degenerate phonon mode at 98.4 and 98.2 $cm^{-1}$, thus assigning them as nearly degenerate (which should not be!).

A discrepancy between experiment and calculation can be seen with the non-degenerate IR-active mode $A_{2u}$. $\omega$ for this phonon mode was 180.5, 61.2, and 71.2 $cm^{-1}$ with Ti_std, Ti_pv, and Ti_sv, respectively. The large difference in the wavenumbers with respect to the PAW potentials can be realized from the phonon dispersion curves shown in Figure 2a−c. From the shape of these curves, it is clear that the phonon modes below 2.5 THz are shallow-like (flattish) around high-symmetry M-point along the path Γ−M−X when the potentials Ti_pv and Ti_sv were used (Figure 2b,c, respectively). This may also mean that a slight distortion of the crystal lattice could cause softening of the phonon mode around the Γ−M−X path. This is not the case with the phonon modes calculated with Ti_std, in which the curves associated with the low-frequency optical modes are relatively steeper (Figure 2a), which match reasonably well with experiment.[81]

When PBE was used, the discrepancies between the phonon modes at low frequencies were very severe. From the data summarized in Table 5, one can see that the frequencies of all the phonon modes are underestimated for all the three PAW potentials utilized. Furthermore, Ti_pv and Ti_sv have predicted soft modes around the Γ-point that are linked with the three IR-active phonon modes and a silent mode; that is, they link with a doubly degenerate mode $E_u$, a non-degenerate mode $A_{2u}$, and a non-degenerate $B_{1u}$ mode. The Ti_pv potential has predicted these phonons at frequencies of 62.8*i*, 106.1*i*, and 30.1*i*, respectively. Similarly, Ti_sv has predicted the corresponding frequencies at 54.4*i*, 98.8*i*, and 16.7*i*, respectively. These soft modes explain why the PBE-relaxed crystal lattice of R-$TiO_2$ is dynamically unstable at the center of the zone, Γ.

Montanari and Harrison[87,88] have demonstrated that the $A_{2u}$ (TO) mode becomes soft at the Γ-point if the crystal of R-$TiO_2$ is expanded via LDA or GGA. This may be consistent with our PBE-level observation. The data suggest that the expansion of the rutile lattice by the two soft potentials softens the phonon modes associated with both the IR-active modes


https://doi.org/10.1021/acsomega.3c02038
ACS Omega 2023, 8, 22003−22017

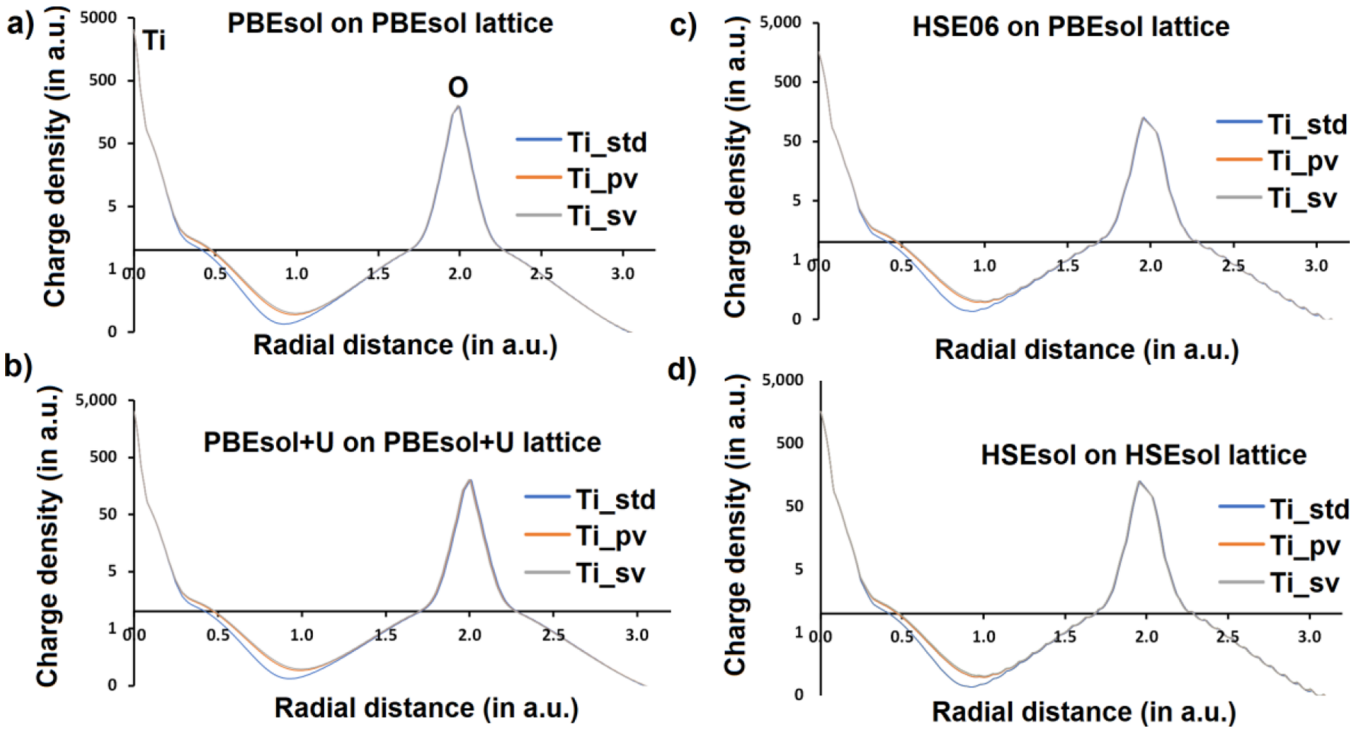


**Figure 6.** 1D plot of the radial dependence of charge density for R-$TiO_2$, evaluated using several methods in combination with the three PAW potentials Ti_std, Ti_sv, and Ti_pv. Charge density calculations were performed on the (a) PBEsol lattice with PBEsol; (b) PBEsol+U lattice with PBEsol+U; (c) HSE06 lattice with PBEsol, and (d) HSEsol lattice with HSEsol. Values are in logarithmic scale.

$E_u$ and $A_{2u}$ (see columns 12 and 14 of Table 5). The lattice expansion is evidenced in Table 1, especially when comparing the lattice parameters evaluated with Ti_std to those with Ti_pv and Ti_sv.

Mitev et al. have also reported an imaginary frequency of 86*i* corresponding to the $A_{2u}$ (TO) phonon mode with the PBE functional using the CASTEP code.[89] We could not reproduce their result because of differing cutoff criteria used in our calculation. The authors of the study have interpreted that the softening of the $A_{2u}$ (TO) mode at the Γ-point could be responsible for the incipient ferroelectric behavior of R-$TiO_2$ and hence should play some role in the determination of large and strongly temperature-dependent dielectric constant.

We now clarify the origin of the spurious (soft) nature of the phonon modes predicted by the two soft potentials Ti_pv and Ti_sv. For this, we investigated the nature of radial dependence of the charge density in one dimension for each of the three PAW potentials. We have used the PBEsol-, PBEsol+U-, and HSEsol-relaxed lattices of R-$TiO_2$. As shown in Figure 6a−d, the nature of the radial dependence of charge density is very similar regardless of the degree of exchange correlation incorporated in each of the DFT methods chosen. That is, the charge density in the region of space between bonded Ti and O atomic basins in R-$TiO_2$, in the close vicinity of Ti, is steep (attractive) when Ti_std was applied and shallow (somehow repulsive!) when Ti_pv and Ti_sv were employed. These results suggest that the softness of the PAW potential (but certainly not the correlation method) is the sole cause of softening of the low-frequency optical phonon modes as a result of increased repulsion between core electrons in the Ti−O bonding region (cf. Figure 2a,b).

A total of 18 phonon modes exist in case of the A-$TiO_2$ lattice.[84,90,91] Of these, 3 are acoustic modes and 15 are optical modes. The irreducible representation of the latter 15 modes is given by $1A_{1g} + 1A_{2u} + 2B_{1g} + 1B_{2u} + 3E_g + 2E_u$. The modes with a subscript "*u*" are IR-active phonon modes except $B_{2u}$ (a silent mode), and those with a subscript "*g*" are Raman-active modes. The PBEsol- and PBE-calculated vibrational frequencies, Table 6, show that the high- and low-frequency phonon modes that are both IR and Raman active are either slightly overestimated or slightly underestimated but were well reproduced by PBEsol in combination with the standard potential Ti_std. In particular, the eight high-frequency Raman and IR modes are all within 15 $cm^{-1}$ of the experimental values. The three doubly degenerate IR and Raman modes ($E_u$ and $E_g$) predicted at frequencies of 240.8 ($E_u$), 164.7 ($E_g$), and 151.4 ($E_g$) $cm^{-1}$ are underestimated or overestimated but all within 35 $cm^{-1}$ of the experimental wavenumbers (Table 6).[84,90] The degree of underestimation of high-frequency phonon vibrations was severe especially with the Ti-centered potentials Ti_pv and Ti_sv; the same behavior was also observed for R-$TiO_2$ (Table 5). As mentioned above, the underestimation should not be due to the short Ti−O bond distance in the crystal lattice calculated using the two soft potentials. We confirmed this by calculating the frequencies of phonon modes with Ti_std, Ti_pv, and Ti_sv using bulk geometries of R- and A-$TiO_2$ obtained with Ti_pv or Ti_sv. As shown in Tables S1 and S2, the phonon frequencies with Ti_std are always higher than those calculated with Ti_pv and Ti_sv, a feature that was emanated irrespective of the type of the crystal lattice used. From this, it is clear that the softer the potential, the shallower the charge density profile in the close vicinity of Ti along the Ti−O bond of $TO_2$, thus softening (lowering) the frequency of phonon vibrations around the zone center. However, the phonon mode softening is less pronounced at the Γ-point for A-$TiO_2$ compared to that found for R-$TiO_2$. The performance of the PBE functional is homologous with that of PBEsol for A-$TiO_2$, but the phonon


https://doi.org/10.1021/acsomega.3c02038
ACS Omega 2023, 8, 22003−22017

Table 7. Comparison of Ionic (Low-Frequency) and Electronic (High-Frequency) Components ($\varepsilon_{ij}^{(0)}$ and $\varepsilon_{ij}^{(\infty)}$, Respectively) of the Relative Dielectric Permittivity Tensor $\varepsilon_r$ of R-$TiO_2$, Obtained Using Three Cutoff Energies in Combination with the PBEsol and Three PAW Potentials Ti_std, Ti_pv, and Ti_sv[a]

| | | $\varepsilon_{ij}^{(0)}$ | | | | $\varepsilon_{ij}^{(\infty)}$ | | | | $\varepsilon_r$ |
|---|---|---|---|---|---|---|---|---|---|---|
| PAW potential | cutoff energy/eV | $\varepsilon_{xx}^{(0)}$ | $\varepsilon_{yy}^{(0)}$ | $\varepsilon_{zz}^{(0)}$ | $\varepsilon_r^{(0)}$ | $\varepsilon_{xx}^{(\infty)}$ | $\varepsilon_{yy}^{(\infty)}$ | $\varepsilon_{zz}^{(\infty)}$ | $\varepsilon_r^{(\infty)}$ | $\varepsilon_r^{(0)} + \varepsilon_r^{(\infty)}$ |
| | | | | R-$TiO_2$ | | | | | | |
| Ti_std | 520.0 | 124.0 | 124.0 | 163.0 | 137.0 | 8.0 | 8.0 | 9.6 | 8.5 | 145.5 |
| | 600.0 | 123.4 | 123.4 | 162.3 | 136.4 | 8.0 | 8.0 | 9.6 | 8.5 | 144.9 |
| | 700.0 | 122.9 | 122.9 | 161.3 | 135.7 | 8.0 | 8.0 | 9.6 | 8.5 | 144.2 |
| Ti_pv | 520.0 | 354.1 | 354.1 | 1135.2 | 614.5 | 7.6 | 7.6 | 9.1 | 8.1 | 622.6 |
| | 600.0 | 366.0 | 366.0 | 1257.8 | 663.3 | 7.6 | 7.6 | 9.1 | 8.1 | 671.3 |
| | 700.0 | 370.3 | 370.3 | 1327.0 | 689.2 | 7.6 | 7.6 | 9.1 | 8.1 | 697.3 |
| Ti_sv | 520.0 | 296.2 | 296.2 | 732.9 | 441.8 | 7.5 | 7.5 | 8.9 | 8.0 | 449.9 |
| | 600.0 | 309.1 | 309.1 | 799.3 | 472.5 | 7.5 | 7.5 | 8.9 | 8.0 | 480.5 |
| | 700.0 | 327.1 | 327.1 | 966.8 | 540.3 | 7.5 | 7.5 | 8.9 | 7.9 | 548.2 |
| expt.[14c] | | 111 | 111 | 257 | 159.7 | | | | | |
| expt.[25] | | 84.69 | 84.69 | 152.97 | 107.45 | 5.96 | 5.96 | 7.16 | 6.36 | 113.81 |
| expt.[85] | | 84.02 | 84.02 | 153.83 | 107.29 | 5.91 | 5.91 | 7.19 | 6.34 | 113.63 |
| expt.[89] | | 81.8 | 81.8 | 167.1 | 110.23 | 6.00 | 6.00 | 7.80 | 6.60 | 116.83 |
| expt.[25] | | 87.0 | 87.0 | 163.0 | 112.33 | 6.12 | 6.12 | 7.63 | 6.62 | 118.96 |
| expt.[25] | | 89.8 | 89.8 | 166.7 | 115.43 | 6.32 | 6.32 | 7.80 | 6.81 | 122.25 |
| expt.[25] | | 86 | 86 | 170 | 114.00 | 6.84 | 6.84 | 8.43 | 7.37 | 121.37 |
| | | | | A-$TiO_2$ | | | | | | |
| Ti_std | 700 | 44.1 | 44.1 | 21.2 | 36.4 | 7.4 | 7.4 | 6.7 | 7.1 | 43.6 |
| Ti_pv | 700 | 54.6 | 54.6 | 23.6 | 44.3 | 7.0 | 7.0 | 6.4 | 6.8 | 51.1 |
| Ti_sv | 700 | 52.4 | 52.4 | 23.3 | 42.7 | 6.9 | 6.9 | 6.3 | 6.7 | 49.4 |
| expt.[92] | | 45.1 | 45.1 | 22.7 | 37.6 | 5.8 | 5.8 | 5.4 | 5.7 | 43.3 |
| | | | | B-$TiO_2$ | | | | | | |
| Ti_std | 700 | 48.2 | 50.7 | 45.0 | 49.4 | 7.6 | 8.0 | 7.4 | 7.7 | 57.2 |
| Ti_pv | 700 | 52.8 | 70.1 | 47.3 | 56.7 | 7.0 | 7.7 | 7.0 | 7.2 | 64.0 |
| Ti_sv | 700 | 52.4 | 68.6 | 47.9 | 56.3 | 6.9 | 7.6 | 6.9 | 7.1 | 63.4 |
| Ref 23[b] | | 64.1 | 86.7 | 55.2 | 68.7 | 6.8 | 7.5 | 6.8 | 7.0 | 75.7 |
| Ref 23[b] | | 50.2 | 58.2 | 50.0 | 52.8 | 7.0 | 7.5 | 6.9 | 7.1 | 59.9 |
| expt.[97,98] | | | | | 93 | | | | | 78 |

[a]Both low- and room-temperature experimental values of $\varepsilon_r$ reported by various authors are included. [b]Reported at the LDA and GGA levels, using Quantum Expresso software. [c]Low-temperature data refer $T$ = 1.6 K.

frequencies are largely underestimated compared to experiment (Table 6).

For B-$TiO_2$, the number of IR- and Raman-active modes is greater than that found in R- and A-$TiO_2$; this is attributed to the greater number of atoms (24) responsible for the unit cell of the brookite lattice. Because of this, and because B-$TiO_2$ has a lower orthorhombic *Pbca* symmetry, there are 36, 24, 9, and 3 Raman-active ($A_{1g}$, $B_{1g}$, $B_{2g}$, and $B_{3g}$), IR-active ($B_{1u}$, $B_{2u}$, $B_{3u}$), silent ($A_{1u}$), and acoustic vibrational phonon modes, respectively. They are represented by the irreducible representations at Γ: $9A_{1g} + 9B_{1g} + 9B_{2g} + 9B_{3g}$, $8B_{1u} + 8B_{2u} + 8B_{3u}$, $9A_{1u}$, and $B_{1u} + B_{2u} + B_{3u}$. The frequencies of the PBEsol- and PBE-calculated phonon modes compared in Table S3 indicate that the phonon modes evaluated with PBEsol with potential Ti_stv are in better agreement with experiment.[84,94]

**3.3. Dependence of the Magnitude of Relative Dielectric Permittivity on PAW Potentials and DFT Methods.** Since rutile and anatase $TiO_2$ are a uniaxial crystal and brookite $TiO_2$ is a biaxial crystal,[95] there are two and three independent non-zero components both for the ionic and electronic parts of the dielectric permittivity, respectively. The average of the former property, $\varepsilon_r^{(0)}$, was added to that of the latter property, $\varepsilon_r^{(\infty)}$, so as to calculate the relative static dielectric permittivity, $\varepsilon_r$, for all the three phases of $TiO_2$. They are summarized in Table 7, together with the experimentally reported values wherever available.

As outlined in the Introduction section, the major controversy of $TiO_2$ lies in the experimental determination and proposed relative dielectric permittivity values of R-$TiO_2$. Some have reported the colossal nature of the ionic and total dielectric permittivities, and others reported appreciably large numbers for the same property for the same system. For instance, Nicolini, in 1952, has proposed a colossal dielectric permittivity of R-$TiO_2$, with $\varepsilon_r$ approximately 10,000 for ceramic R-$TiO_2$. This value is close to the range 100−10,000 reported by Parker and Wasilik,[12] as well as by Chu.[13] Parker and Wasilik[12] have reported a colossal dielectric permittivity in hydrogenated and reduced oxygen-rich rutile single crystalline $TiO_2$ [e.g., Nicolini ($\varepsilon_r$ = 10,000) and Perker et al. ($\varepsilon_r$ = (10,000−30,000)]. Later, in 1961, Parker reported values of 111 and 257 for $\varepsilon_\perp^{(0)} = \varepsilon_{xx}^{(0)} = \varepsilon_{yy}^{(0)}$ and $\varepsilon_\parallel^{(0)} = \varepsilon_{zz}^{(0)}$ along the crystallographic *a*−/*b*- and *c*-axes of R-$TiO_2$ at low temperature, 1.6 K, respectively; these were 86 (58) and 170 (97) at 300 (1000) K, respectively.[14] Indeed, these results were in agreement with Samara and Peercy [$\varepsilon_r$ values along the *a*- and *c*-axes were 89.8 (114.9) and 166.7 (251) at 296 K (4 K), respectively].[24] Bonkerud et al.[16] have recently argued that they fail to confirm the results of Nicolini[11] and Parker and Wasilik,[12] even though they could reconfirm the results


https://doi.org/10.1021/acsomega.3c02038
ACS Omega 2023, 8, 22003−22017

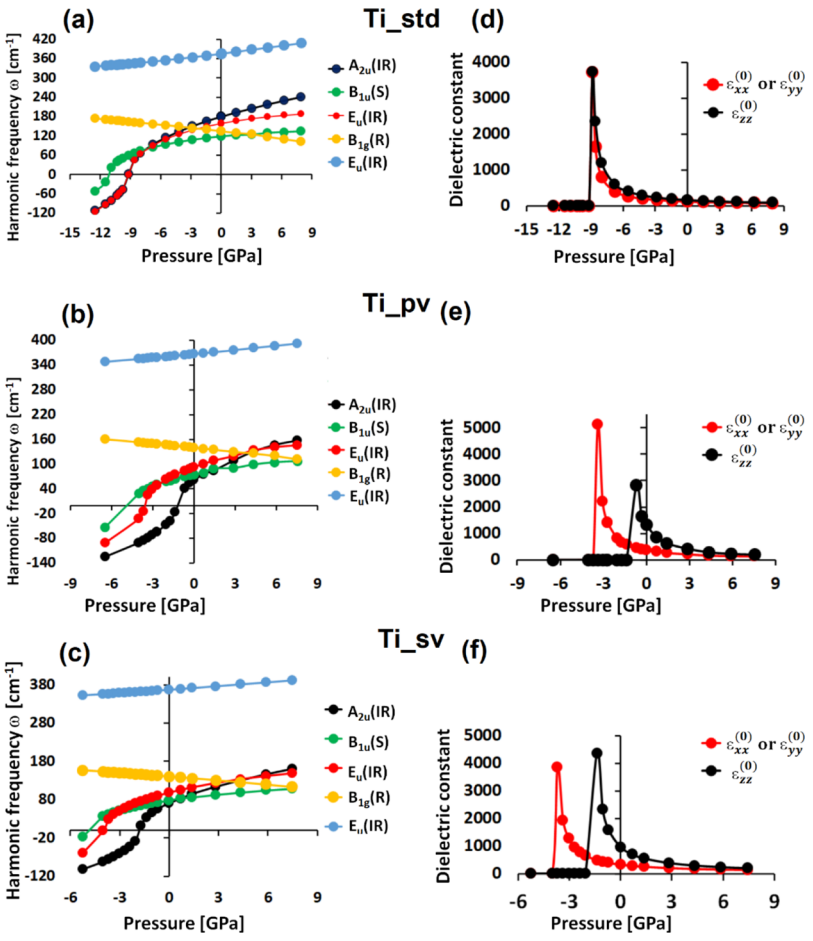


**Figure 7.** (Left) PBEsol level external (hydrostatic) pressure dependence of the lowest five Γ-centered phonon modes of R-$TiO_2$, obtained with PAW potentials: (a) Ti_std; (b) Ti_pv; (c) Ti_sv. (Right) The dependence of dielectric permittivity (ionic) on applied pressure, obtained PAW potentials: (d) Ti_std; (e) Ti_pv; and (f) Ti_sv. The labeling of the phonon modes is consistent with the data shown in Table 5.

individually published by Parker[14] and Samara and Peercy.[24] Therefore, the anomalous dielectric permittivity reported by various authors has continuously been debated since some of the reported results above are the repercussion of any incorrectly designed experiment or an incorrect interpretation.

The trend in our PBEsol-based values of $\varepsilon_{\perp}^{(0)}$ ($\varepsilon_{\perp}^{(0)} = [\varepsilon_{xx}^{(0)} + \varepsilon_{yy}^{(0)}]/2$) and $\varepsilon_{\parallel}^{(0)}$ ($\varepsilon_{\parallel}^{(0)} = \varepsilon_{zz}^{(0)}$) (Table 7) calculated with Ti_std is in agreement with those of Samara and Peercy,[24] and Parker,[14] as well as of Bonkerud et al.[16] Because Ti_pv and Ti_sv underestimate wavenumbers of the low-frequency phonons (Table 5) compared to Ti_std, they are the cause of spuriously large $\varepsilon_r^{(0)}$ for R-$TiO_2$. The feature is persistent regardless of the three energy cutoff values invoked during our calculation (Table 7). The discrepancy is understandable since the calculation of the dielectric permittivity due to ions strongly relies on the nature of the PAW potential responsible for the determination of the positive eigenvalues of the dynamical matrix, and the low-frequency phonon mode is the main factor in determining the net magnitude of $\varepsilon_r^{(0)}$. The latter is not surprising given that the $\varepsilon_r^{(0)}$ is inversely proportional to the square of the phonon frequency ($\varepsilon_r^{(0)} \alpha 1/\omega^2$),[96] so that the smaller the phonon frequency, the larger the value of $\varepsilon_r^{(0)}$. The notion is consistent with the rule of thumb that the combination of a higher frequency and a lower polarization factor should result in a lower dielectric constant in any specific direction. By contrast, $\varepsilon_r^{(\infty)}$ is nearly invariant with respect to the cutoff energies used.

Table S4 summarizes $\varepsilon_r^{(0)}$ and $\varepsilon_r^{(\infty)}$ of R-$TiO_2$, calculated using PBE. The data reveal that neither of the three PAW potentials, in combination with the three energy cutoffs utilized, are suitable in reproducing experimental $\varepsilon_r^{(0)}$. The $\varepsilon_r^{(0)}$ was predicted to be spuriously large ($\varepsilon_r^{(0}$ in the range 415−421) with Ti_std and unphysical with Ti_sv and Ti_pv. The $\varepsilon_r^{(\infty)}$ values (e.g., 7.9, 8.1, and 8.6 with Ti_sv, Ti_pv, and Ti, respectively) are slightly overestimated relative to the experimentally suggested range ($\varepsilon_r^{(\infty)}$ between 6.3 and 7.4).

We have calculated $\varepsilon_r^{(0)}$ and $\varepsilon_r^{(\infty)}$ using PBE+U and PBEsol +U (U = 3.0 eV). This was instigated with the perception that the inclusion of the Hubbard on-site effective potential U centered on the d-orbital of the Ti atom provides the expected chemistry of localized electrons and hole polarons and their energetics for rutile, anatase, and brookite $TiO_2$ and that the GGA alone fails to do so.[99−101] The $\varepsilon_r^{(0)}$ and $\varepsilon_r^{(\infty)}$ values in Table S5, show, first, that $\varepsilon_{ij}^{(0)}$ and $\varepsilon_{ij}^{(\infty)}$ computed with a specific functional are largely unaffected changing the cutoff energy for a particular PAW potential. Second, when moving from Ti_std through Ti_pv to Ti_sv, there is a systematic increase in the magnitude of both $\varepsilon_{ij}^{(0)}$ and $\varepsilon_{ij}^{(\infty)}$ for a specific functional and cutoff energy. Third, the GGA-based mean value of $\varepsilon_{ij}^{(0)}$ is roughly two or three times smaller when computed with DFT+U ($\varepsilon_{ij}^{(0)}$ in the range 44−69 (35−54) with PBE+U (PBEsol+U)), so there is a sharp disagreement between the calculated and experimental values of $\varepsilon_r^{(0)}$. Similarly, the DFT+U-calculated difference between the


https://doi.org/10.1021/acsomega.3c02038
ACS Omega 2023, 8, 22003−22017

parallel and perpendicular components of $\varepsilon_{ij}^{(0)}$ is also unphysically small compared to the notable difference deduced from the corresponding experimental values. Fourth, the $\varepsilon_{ij}^{(\infty)}$ are almost oblivious with respect to the two DFT+U methods applied for any particular potential and cutoff energy and are close to the experimental range of reported values (6.3−7.4, see Table 7). The only feature that manifests with the combination between the Hubbard term and DFT is the disappearance of all soft (low-frequency IR-active) phonon modes, meaning that the combination does not predict the dynamic instability of the R-$TiO_2$ lattice predicted by Ti_pv and Ti_sv in combination with PBE (Table 6).

Tables 6 and S4 list the PBEsol- and PBE-calculated $\varepsilon_r^{(0)}$, $\varepsilon_r^{(\infty)}$, and $\varepsilon_r$ values for A- and B-$TiO_2$, respectively. For A-$TiO_2$, PBEsol/Ti_std shows the best prediction of $\varepsilon_r$ ($\varepsilon_r$ = 43.6 with PBEsol/Ti_std and 43.3 with experiment). This is compared to those predicted byPBEsol/Ti_pv and PBEsol/Ti_sv that have overestimated $\varepsilon_r$ by 7.8 and 6.1, respectively. The corresponding overestimations by PBE were 10.5, 20.0, and 18.5 for Ti_std, Ti_pv, and Ti_sv, respectively. These values are indeed large, appearing due to numerically small frequencies associated with the low-frequency phonon modes. The lack of detailed experimental data for B-$TiO_2$ did not allow us to estimate the performance of PAW potentials and correlation methods in predicting the accuracy of $\varepsilon_r$ values.

Our result suggests that the $\varepsilon_r$ value for the R-$TiO_2$ lattice is larger than that of the A- and B-$TiO_2$ lattices ($\varepsilon_r$(R) < $\varepsilon_r$(B) < $\varepsilon_r$(A)). For mass density, $\rho$(A) < $\rho$(B) < $\rho$(R).

The ionic and optical dielectric constants for the two cubic phases of $TiO_2$ are listed in Table S6. The former could not be determined correctly and are unphysical, even though the large values of $\varepsilon_r^{(0)}$ indicate the presence of any ferroelectric transition. The obvious reason for this is that the frequencies of the three low-frequency phonon modes were too small for F-$TiO_2$, and many of them were negative for P-$TiO_2$. The optical dielectric constant was close to 10.0−11.0 for both the systems. They are larger than those calculated for R-, A-, and B-$TiO_2$.

We found that $\varepsilon_\perp^{(0)} < \varepsilon_\parallel^{(0)}$ for R-$TiO_2$ with PBEsol; it is reversed ($\varepsilon_\perp^{(0)} > \varepsilon_\parallel^{(0)}$) for A-$TiO_2$. The anisotropic nature of $\varepsilon_r^{(0)}$ is similar to that found for the electronic part of $\varepsilon_r$ (i.e., $\varepsilon_\perp^{(\infty)} < \varepsilon_\parallel^{(\infty)}$ for R-$TiO_2$; $\varepsilon_\perp^{(\infty)} < \varepsilon_\parallel^{(\infty)}$ for A-$TiO_2$), showing that the polarization along the c-direction is strongest for the former than for the latter system. This may indicate that the excitonic wavefunctions are extended in one direction than the remaining two, which are expected of low-dimensional excitons.[21] As mentioned by Mikami et al.,[90] Wemple[102] has observed that the difference between the dielectric permittivity of the two $TiO_2$ phases was due to the smaller anion density of anatase $TiO_2$.

We have calculated the dielectric permittivity and phonon frequencies for R-$TiO_2$ using the relaxed lattices of HSEsol and HSE06, in which the frozen phonon approximation was invoked. The results are summarized in Tables S7 and S8. As observed with GGA (see above), the HSE results show that the magnitude of $\varepsilon^{(0)}$ depends significantly on the type of the PAW potential employed. Overall, the $\varepsilon^{(0)}$ value of [HSE06/Ti_std] agrees well with low-temperature experimental results discussed above.[14] The $\varepsilon^{(\infty)}$ values are also in better agreement with experiment due to a systematic improvement of the band gap with the HSE methods.

### 3.4. Dependence of Low-Frequency Phonon Modes and Static Dielectric Constant on Hydrostatic Pressure.

We have examined the isotropic pressure dependence of the geometry, zone-center phonon modes, and relative dielectric constant of R-$TiO_2$. Figure 7a−c shows the dependence of the harmonic frequencies of the lowest five Γ-center phonon modes on the applied pressure of R-$TiO_2$. Except for the degenerate IR-active mode $E_u$ ($\omega$ = 375.0 $cm^{-1}$ with PBEsol/Ti_std) and the non-degenerate Raman-active mode $B_{1g}$ ($\omega$ = 134.2 $cm^{-1}$ with PBEsol/Ti_std), the phonon frequencies of the other three IR-active bands with mode symmetry $A_{2u}$, $B_{1u}$, and $E_u$ are affected by applied pressure. Figure 7 That is, ferroelectricity can be induced to the rutile lattice of $TiO_2$ via negative hydrostatic pressure, and the most sensitive ferroelectric mode is the TO mode $A_{2u}$. The other two modes ($B_{1u}$ and $E_u$) soften as the pressure increases, which causes further expansion of the rutile lattice. The softness of the $E_u$ mode, which is the analogue of the $A_{2u}$ mode in the $a$−$b$ plane, was previously observed.[87]

The three PAW potentials give qualitatively similar insight into the development of the three ferroelectric modes, thus leading to the creativity of lattice instability. However, the application of the two soft potentials Ti_pv and Ti_sv confirms that the phonon frequency of the $A_{2u}$ mode vanishes faster than that of the $B_{1u}$ and $E_u$ modes and becomes more negative when the lattice is expanded. That is, for the PAW potentials Ti_pv and Ti_sv, the frequency of the $A_{2u}$ mode vanishes at hydrostatic pressure at about −1.0 GPa, while it is about −9.3 GPa with Ti_std. These results explain why the static dielectric constant increases dramatically and more rapidly with Ti_pv and Ti_sv compared to Ti_std, which may be captured from Figure 7d−f. Also, the anisotropy in the in- and out-of-plane dielectric constants predicted with the two soft potentials are quite significant than that predicted using Ti_std. The component of dielectric constant parallel to the $c$-axis is increased prominently compared to the in-plane dielectric constants for all the three occasions exploited, meaning that an enhancement of the dielectric constant can be made possible via the expansion of the rutile lattice of $TiO_2$.

## 4. CONCLUSIONS

This study has utilized three most commonly used variants of the PAW potential for Ti to examine the physical properties of $TiO_2$. In particular, the combined application of these pseudopotentials with PBE, PBEsol, and PBEsol+U has enabled us to assess the accuracy of the ground-state lattice properties, phonon vibrations, and relative static dielectric permittivity. We have shown that the change in the size of the potential can have a non-negligible effect on the temperature-dependent lattice geometry of all the five phases of $TiO_2$. Their effect is particularly pronounced when the low frequencies of optical phonon modes, as well as the ionic contribution to the relative dielectric permittivity, were compared. The origin of the underlying difference was uncovered when radial dependence of the charge density was analyzed around the close vicinity of Ti. We have argued that the radial dependence of charge density is relatively steep in the close vicinity of Ti when the standard potential Ti_std was invoked; it was shallow when the two soft potentials Ti_pv and Ti_sv were invoked. Because of this nature of the charge density profile, Ti_std has produced higher phonon frequencies (and relatively accurate $\varepsilon_r^{(0)}$) than that predicted with Ti_pv and Ti_sv. Higher-level calculations using HSEsol and HSE06 have shown to have some improvement on the accuracy of the dielectric properties, despite being computationally intensive. In


https://doi.org/10.1021/acsomega.3c02038
ACS Omega 2023, 8, 22003−22017

addition, we have shown that ferroelectric instability can be induced in the R-$TiO_2$ lattice by applying negative hydrostatic pressure. At least three low-lying phonon modes ($A_{2u}$, $B_{1u}$, and $E_u$) of R-$TiO_2$ are observed to be sensitive not only to the onset of ferroelectric phase transitions but also to the hard and soft nature of the three PAW potentials. Finally, we recommend using the standard PAW potential, Ti_std, for modeling the ground-state lattice properties and phonon-related features of $TiO_2$-based materials, rather than choosing a softer PAW potential.

## ■ ASSOCIATED CONTENT

### Data Availability Statement

This research did not report any data.

### Supporting Information

The Supporting Information is available free of charge at https://pubs.acs.org/doi/10.1021/acsomega.3c02038.

Comparison of the IR and Raman frequencies $\omega$ ($cm^{-1}$) and IR intensities $I$ (km/mol) obtained using PBEsol in combination with PAW potentials Ti_std, Ti_pv, and Ti_sv centered on Ti of R-$TiO_2$; comparison of the IR and Raman frequencies $\omega$ ($cm^{-1}$) and IR intensities $I$ (km/mol) obtained using PBEsol in combination with PAW potentials Ti_std, Ti_pv, and Ti_sv centered on Ti of R-$TiO_2$; comparison of the IR and Raman frequencies and IR intensities obtained using PBEsol and PBE functionals, in conjunction with PAW potentials Ti_std, Ti_pv, and Ti_sv centered on Ti of B-$TiO_2$; comparison of the PBE level electronic and ionic components ($\varepsilon_{ij}^{(0)}$ and $\varepsilon_{ij}^{(\infty)}$, respectively) of the relative dielectric permittivity tensor $\varepsilon_{ij}$ for R- and A-$TiO_2$, computed in conjunction with three variants of the PAW potential, viz., Ti_std, Ti_pv, and Ti_sv; comparison of the PBE+U and PBEsol+U (U = 3.0 eV) level electronic and ionic components ($\varepsilon_{ij}^{(0)}$ and $\varepsilon_{ij}^{(\infty)}$, respectively) of the relative dielectric permittivity tensor $\varepsilon_r$ for R-$TiO_2$, computed in conjunction with three variants of the PAW potential, viz., Ti_std, Ti_pv, and Ti_sv; comparison of the PBEsol level electronic and ionic components ($\varepsilon_{ij}^{(0)}$ and $\varepsilon_{ij}^{(\infty)}$, respectively) of the relative dielectric permittivity tensor $\varepsilon_{ij}$ for F- and P-$TiO_2$, computed in conjunction with three variants of the PAW potential, viz., Ti_std, Ti_pv, and Ti_sv; ionic (low-frequency) and electronic (high-frequency) components ($\varepsilon_{ij}^{(0)}$ and $\varepsilon_{ij}^{(\infty)}$, respectively) of the dielectric permittivity tensor $\varepsilon_r$ of R-$TiO_2$, obtained using HSEsol and HSE06 in combination with the three PAW potentials Ti_std; and comparison of the IR and Raman frequencies $\omega$ ($cm^{-1}$) obtained using HSEsol and HSE06 in combination with PAW potentials Ti_std centered on Ti of R-$TiO_2$ (PDF)

## ■ AUTHOR INFORMATION


### Corresponding Authors

**Pradeep R. Varadwaj** − *Institute of Innovation for Future Society, Nagoya University, Nagoya 464-8601, Japan; Molecular Sciences Institute, School of Chemistry, University of the Witwatersrand, Johannesburg 2050, South Africa;* orcid.org/0000-0002-7102-3133; Email: pradeep@chem.material.nagoya-u.ac.jp, prv.aist@gmail.com

**Ryoji Asahi** − *Institute of Innovation for Future Society, Nagoya University, Nagoya 464-8601, Japan;* orcid.org/0000-0002-2658-6260; Email: ryoji.asahi@chem.material.nagoya-u.ac.jp

### Authors

**Van An Dinh** − *Department of Precision Engineering, Graduate School of Engineering, Osaka University, Suita, Osaka 565-0871, Japan*

**Yoshitada Morikawa** − *Department of Precision Engineering, Graduate School of Engineering, Osaka University, Suita, Osaka 565-0871, Japan;* orcid.org/0000-0003-4895-4121

Complete contact information is available at: https://pubs.acs.org/10.1021/acsomega.3c02038


### Author Contributions

Conceptualization, P.R.V.; computation, data acquisition, formal analysis, and investigation, P.R.V.; computation of phonon modes of R-, A-, and B-$TiO_2$: R.A.; computational verifications and critical discussions, V.A.D. and Y.M.; supervision, R.A.; drawing of figures, preparation of tables, and writing—original draft, P.R.V.; writing—review and editing, P.R.V. and R.A.; All authors have read and agreed to the published version of the manuscript.


### Funding

This research was funded by JSPS Grant-in-Aid for Transformative Research Areas (A); Grant numbers: 21H05560 and 20H05883.


### Notes

The authors declare no competing financial interest.

## ■ ACKNOWLEDGMENTS


This work was entirely conducted using the computation and laboratory facilities provided by the University of Nagoya and the Research Center for Computational Science,, Okazaki, Japan (Project: 22-IMS-C099). P.R.V. has been appointed as a Reader of the University of Witwatersrand (SA). R.A. thanks Drs. Hiroki Taniguchi and Koichi Hayashi for their fruitful discussions.


## ■ REFERENCES


(1) Muscat, J.; Swamy, V.; Harrison, N. M. First-Principles Calculations of the Phase Stability of $TiO_2$. *Phys. Rev. B* **2002**, *65*, No. 224112.

(2) Daβler, A.; Feltz, A.; Jung, J.; Ludwig, W.; Kaisersberger, E. Characterization of Rutile and Anatase Powders by Thermal Analysis. *J. Therm. Anal.* **1988**, *33*, 803−809.

(3) Dambournet, D.; Belharouak, I.; Amine, K. Tailored Preparation Methods of $TiO_2$ Anatase, Rutile, Brookite: Mechanism of Formation and Electrochemical Properties. *Chem. Mater.* **2010**, *22*, 1173−1179.

(4) Li, J.-G.; Ishigaki, T. Brookite̅rutile Phase Transformation of TiO2 Studied with Monodispersed Particles. *Acta Mater.* **2004**, *52*, 5143−5150.

(5) Pascual, J.; Camassel, J.; Mathieu, H. Fine Structure in the Intrinsic Absorption Edge of $TiO_2$. *Phys. Rev. B* **1978**, *18*, 5606−5614.

(6) Allen, N. S.; Mahdjoub, N.; Vishnyakov, V.; Kelly, P. J.; Kriek, R. J. The Effect of Crystalline Phase (Anatase, Brookite and Rutile) and Size on the Photocatalytic Activity of Calcined Polymorphic Titanium Dioxide ($TiO_2$). *Polym. Degrad. Stab.* **2018**, *150*, 31−36.

(7) Tang, H.; Lévy, F.; Berger, H.; Schmid, P. E. Urbach Tail of Anatase $TiO_2$. *Phys. Rev. B* **1995**, *52*, 7771−7774.

(8) Mattsson, A.; Österlund, L. Adsorption and Photoinduced Decomposition of Acetone and Acetic Acid on Anatase, Brookite, and Rutile TiO2 Nanoparticles. *J. Phys. Chem. C* **2010**, *114*, 14121−14132.

(9) Carp, O.; Huisman, C. L.; Reller, A. Photoinduced Reactivity of Titanium Dioxide. *Prog. Solid State Chem.* **2004**, *32*, 33−177.
(10) Gyanan; Mondal, S.; Kumar, A. Tunable Dielectric Properties of $TiO_2$ Thin Film Based MOS Systems for Application in Microelectronics. *Superlattices Microstruct.* **2016**, *100*, 876−885.
(11) Nicolini, L. A New Dielectric Material. *Nature* **1952**, *170*, 938−938.
(12) Parker, R. A.; Wasilik, J. H. Dielectric Constant and Dielectric Loss of $TiO_2$ (Rutile) at Low Frequencies. *Phys. Rev.* **1960**, *120*, 1631−1637.
(13) Chu, C. W. New Ordered Phases of Slightly Reduced Rutile and Their Sharp Dielectric Absorptions at Low Temperature. *Phys. Rev. B* **1970**, *1*, 4700−4708.
(14) Parker, R. A. Static Dielectric Constant of Rutile ($TiO_2$), 1.6-1060 °K. *Phys. Rev.* **1961**, *124*, 1719−1722.
(15) Peercy, P. S.; Morosin, B. Pressure and Temperature Dependences of the Raman-Active Phonons in $SnO_2$. *Phys. Rev. B* **1973**, *7*, 2779−2786.
(16) Bonkerud, J.; Zimmermann, C.; Weiser, P. M.; Vines, L.; Monakhov, E. V. On the Permittivity of Titanium Dioxide. *Sci. Rep.* **2021**, *11*, 12443.
(17) Tse, M.-Y.; Wei, X.; Hao, J. High-Performance Colossal Permittivity Materials of (Nb + Er) Co-Doped $TiO_2$ for Large Capacitors and High-Energy-Density Storage Devices. *Phys. Chem. Chem. Phys.* **2016**, *18*, 24270−24277.
(18) Kawarasaki, M.; Tanabe, K.; Terasaki, I.; Fujii, Y.; Taniguchi, H. Intrinsic Enhancement of Dielectric Permittivity in (Nb + In) Co-Doped $TiO_2$ Single Crystals. *Sci. Rep.* **2017**, *7*, 5351.
(19) Elshahawy, A. M.; Elkatlawy, S. M.; Shalaby, M. S.; Guan, C.; Wang, J. Surface-Engineered $TiO_2$ for High-Performance Flexible Supercapacitor Applications. *J. Electron. Mater.* **2023**, *52*, 1347−1356.
(20) Osada, M.; Kobayashi, M.; Kakihana, M. Enhanced Dielectric Response Induced by Controlled Morphology in Rutile $TiO_2$ Nanocrystals. *J. Ceram. Soc. Jpn.* **2013**, *121*, 593−597.
(21) Thilagam, A.; Simpson, D. J.; Gerson, A. R. A First-Principles Study of the Dielectric Properties of $TiO_2$ polymorphs. *J. Phys.: Condens. Matter* **2011**, *23*, No. 025901.
(22) Mahmood, T.; Malik, H.; Batool, R.; Perveen, Z.; Saleemi, F.; Rasheed, H.; Saeed, M. A.; Cao, C.; Rizwan, M. Elastic, Electronic and Optical Properties of Anatase $TiO_2$ under Pressure: A DFT Approach. *Chin. J. Phys.* **2017**, *55*, 1252−1263.
(23) Shojaee, E.; Abbasnejad, M.; Saeedian, M.; Mohammadizadeh, M. R. First-Principles Study of Lattice Dynamics of $TiO_2$ in Brookite and Cotunnite Structures. *Phys. Rev. B* **2011**, *83*, No. 174302.
(24) Samara, G. A.; Peercy, P. S. Pressure and Temperature Dependence of the Static Dielectric Constants and Raman Spectra of $TiO_2$ (Rutile). *Phys. Rev. B* **1973**, *7*, 1131−1148.
(25) Schöche, S.; Hofmann, T.; Korlacki, R.; Tiwald, T. E.; Schubert, M. Infrared Dielectric Anisotropy and Phonon Modes of Rutile $TiO_2$. *J. Appl. Phys.* **2013**, *113*, 164102.
(26) Ke, S.; Li, T.; Ye, M.; Lin, P.; Yuan, W.; Zeng, X.; Chen, L.; Huang, H. Origin of Colossal Dielectric Response in (In + Nb) Co-Doped $TiO_2$ Rutile Ceramics: A Potential Electrothermal Material. *Sci. Rep.* **2017**, *7*, 10144.
(27) Zhao, C.; Wu, J. Effects of Secondary Phases on the High-Performance Colossal Permittivity in Titanium Dioxide Ceramics. *ACS Appl. Mater. Interfaces* **2018**, *10*, 3680−3688.
(28) Hu, W.; Lau, K.; Liu, Y.; Withers, R. L.; Chen, H.; Fu, L.; Gong, B.; Hutchison, W. Colossal Dielectric Permittivity in (Nb+Al) Codoped Rutile $TiO_2$ Ceramics: Compositional Gradient and Local Structure. *Chem. Mater.* **2015**, *27*, 4934−4942.
(29) Lee, B.; Lee, C.; Hwang, C. S.; Han, S. Influence of Exchange-Correlation Functionals on Dielectric Properties of Rutile $TiO_2$. *Curr. Appl. Phys.* **2011**, *11*, S293−S296.
(30) Dou, M.; Persson, C. Comparative Study of Rutile and Anatase $SnO_2$ and $TiO_2$: Band-Edge Structures, Dielectric Functions, and Polaron Effects. *J. Appl. Phys.* **2013**, *113*, No. 083703.
(31) Skone, J. H.; Govoni, M.; Galli, G. Self-Consistent Hybrid Functional for Condensed Systems. *Phys. Rev. B* **2014**, *89*, No. 195112.
(32) Gerosa, M.; Bottani, C. E.; Di Valentin, C.; Onida, G.; Pacchioni, G. Accuracy of Dielectric-Dependent Hybrid Functionals in the Prediction of Optoelectronic Properties of Metal Oxide Semiconductors: A Comprehensive Comparison with Many-Body *GW* and Experiments. *J. Phys.: Condens. Matter* **2018**, *30*, No. 044003.
(33) Gerosa, M.; Bottani, C. E.; Caramella, L.; Onida, G.; Di Valentin, C.; Pacchioni, G. Electronic Structure and Phase Stability of Oxide Semiconductors: Performance of Dielectric-Dependent Hybrid Functional DFT, Benchmarked against GW Band Structure Calculations and Experiments. *Phys. Rev. B* **2015**, *91*, No. 155201.
(34) Lee, C.; Ghosez, P.; Gonze, X. Lattice Dynamics and Dielectric Properties of Incipient Ferroelectric $TiO_2$ Rutile. *Phys. Rev. B* **1994**, *50*, 13379−13387.
(35) Wehinger, B.; Bosak, A.; Jochym, P. T. Soft Phonon Modes in Rutile $TiO_2$. *Phys. Rev. B* **2016**, *93*, No. 014303.
(36) Perdew, J. P.; Ruzsinszky, A.; Csonka, G. I.; Vydrov, O. A.; Scuseria, G. E.; Constantin, L. A.; Zhou, X.; Burke, K. Restoring the Density-Gradient Expansion for Exchange in Solids and Surfaces. *Phys. Rev. Lett.* **2008**, *100*, No. 136406.
(37) Perdew, J. P.; Burke, K.; Ernzerhof, M. Generalized Gradient Approximation Made Simple. *Phys. Rev. Lett.* **1996**, *77*, 3865−3868.
(38) Perdew, J. P.; Burke, K.; Ernzerhof, M. Generalized Gradient Approximation Made Simple [Phys. Rev. Lett. 77, 3865 (1996)]. *Phys. Rev. Lett.* **1997**, *78*, 1396−1396.
(39) Dudarev, S. L.; Botton, G. A.; Savrasov, S. Y.; Humphreys, C. J.; Sutton, A. P. Electron-Energy-Loss Spectra and the Structural Stability of Nickel Oxide: An LSDA+U Study. *Phys. Rev. B* **1998**, *57*, 1505−1509.
(40) Liechtenstein, A. I.; Anisimov, V. I.; Zaanen, J. Density-Functional Theory and Strong Interactions: Orbital Ordering in Mott-Hubbard Insulators. *Phys. Rev. B* **1995**, *52*, R5467−R5470.
(41) Gajdoš, M.; Hummer, K.; Kresse, G.; Furthmüller, J.; Bechstedt, F. Linear Optical Properties in the Projector-Augmented Wave Methodology. *Phys. Rev. B* **2006**, *73*, No. 045112.
(42) Wu, X.; Vanderbilt, D.; Hamann, D. R. Systematic Treatment of Displacements, Strains, and Electric Fields in Density-Functional Perturbation Theory. *Phys. Rev. B* **2005**, *72*, No. 035105.
(43) Pérez-Osorio, M. A.; Milot, R. L.; Filip, M. R.; Patel, J. B.; Herz, L. M.; Johnston, M. B.; Giustino, F. Vibrational Properties of the Organic−Inorganic Halide Perovskite $CH_3NH_3PbI_3$ from Theory and Experiment: Factor Group Analysis, First-Principles Calculations, and Low-Temperature Infrared Spectra. *J. Phys. Chem. C* **2015**, *119*, 25703−25718.
(44) Dharmale, N.; Chaudhury, S.; Mahamune, R.; Dash, D. Comparative Study on Structural, Electronic, Optical and Mechanical Properties of Normal and High Pressure Phases Titanium Dioxide Using DFT. *Mater. Res. Express* **2020**, *7*, No. 054004.
(45) Swamy, V.; Muddle, B. C. Ultrastiff Cubic $TiO_2$ Identified via First-Principles Calculations. *Phys. Rev. Lett.* **2007**, *98*, No. 035502.
(46) Liang, Y.; Zhang, B.; Zhao, J. Mechanical Properties and Structural Identifications of Cubic $TiO_2$. *Phys. Rev. B* **2008**, *77*, No. 094126.
(47) Niu, M.; Cheng, D.; Cao, D. Fluorite $TiO_2$(111) Surface Phase for Enhanced Visible-Light Solar Energy Conversion. *J. Phys. Chem. C* **2014**, *118*, 20107−20111.
(48) Abbasnejad, M.; Shojaee, E.; Mohammadizadeh, M. R.; Alaei, M.; Maezono, R. Quantum Monte Carlo Study of High-Pressure Cubic $TiO_2$. *Appl. Phys. Lett.* **2012**, *100*, 261902.
(49) Kresse, G.; Hafner, J. Norm-Conserving and Ultrasoft Pseudopotentials for First-Row and Transition Elements. *J. Phys.: Condens. Matter* **1994**, *6*, 8245−8257.
(50) Kresse, G.; Joubert, D. From Ultrasoft Pseudopotentials to the Projector Augmented-Wave Method. *Phys. Rev. B* **1999**, *59*, 1758−1775.
(51) Kresse, G.; Hafner, J. Ab Initio Molecular Dynamics for Liquid Metals. *Phys. Rev. B* **1993**, *47*, 558−561.


https://doi.org/10.1021/acsomega.3c02038
*ACS Omega* 2023, 8, 22003−22017

(52) Kresse, G.; Furthmüller, J. Efficiency of Ab-Initio Total Energy Calculations for Metals and Semiconductors Using a Plane-Wave Basis Set. *Comput. Mater. Sci.* **1996**, *6*, 15−50.
(53) Kresse, G.; Furthmüller, J. Efficient Iterative Schemes for Ab Initio Total-Energy Calculations Using a Plane-Wave Basis Set. *Phys. Rev. B* **1996**, *54*, 11169−11186.
(54) Krukau, A. V.; Vydrov, O. A.; Izmaylov, A. F.; Scuseria, G. E. Influence of the Exchange Screening Parameter on the Performance of Screened Hybrid Functionals. *J. Chem. Phys.* **2006**, *125*, 224106.
(55) Schimka, L.; Harl, J.; Kresse, G. Improved Hybrid Functional for Solids: The HSEsol Functional. *J. Chem. Phys.* **2011**, *134*, No. 024116.
(56) Bokdam, M.; Sander, T.; Stroppa, A.; Picozzi, S.; Sarma, D. D.; Franchini, C.; Kresse, G. Role of Polar Phonons in the Photo Excited State of Metal Halide Perovskites. *Sci. Rep.* **2016**, *6*, 28618.
(57) *Dielectric and ferroic properties of metal halide perovskites | APL Materials*; AIP Publishing. https://pubs.aip.org/aip/apm/article/7/1/010901/1062013/Dielectric-and-ferroic-properties-of-metal-halide (accessed May 8, 2023).
(58) Brivio, F.; Walker, A. B.; Walsh, A. Structural and Electronic Properties of Hybrid Perovskites for High-Efficiency Thin-Film Photovoltaics from First-Principles. *APL Mater.* **2013**, *1*, No. 042111.
(59) Varadwaj, P. R.; Marques, H. M. The $Cs_2AgRhCl_6$ Halide Double Perovskite: A Dynamically Stable Lead-Free Transition-Metal Driven Semiconducting Material for Optoelectronics. *Front. Chem.* **2020**, *8*, 796.
(60) Cockayne, E.; Burton, B. P. Phonons and Static Dielectric Constant in $CaTiO_3$ from First Principles. *Phys. Rev. B* **2000**, *62*, 3735−3743.
(61) Cockayne, E. Comparative Dielectric Response in $CaTiO_3$ and $CaAl_{1/2}Nb_{1/2}O_3$ from First Principles. *J. Appl. Phys.* **2001**, *90*, 1459−1468.
(62) Umari, P.; Pasquarello, A. Ab Initio Molecular Dynamics in a Finite Homogeneous Electric Field. *Phys. Rev. Lett.* **2002**, *89*, No. 157602.
(63) Parlinski, K.; Li, Z. Q.; Kawazoe, Y. First-Principles Determination of the Soft Mode in Cubic $ZrO_2$. *Phys. Rev. Lett.* **1997**, *78*, 4063−4066.
(64) Parlinski, K.; Piekarz, P. Ab Initio Determination of Raman Spectra of $Mg_2SiO_4$ and $Ca_2MgSi_2O_7$ Showing Mixed Modes Related to LO/TO Splitting. *J. Raman Spectrosc.* **2021**, *52*, 1346−1359.
(65) Togo, A.; Tanaka, I. First Principles Phonon Calculations in Materials Science. *Scr. Mater.* **2015**, *108*, 1−5.
(66) Mashimo, T.; Bagum, R.; Ogata, Y.; Tokuda, M.; Okube, M.; Sugiyama, K.; Kinemuchi, Y.; Isobe, H.; Yoshiasa, A. Structure of Single-Crystal Rutile ($TiO_2$) Prepared by High-Temperature Ultra-centrifugation. *Cryst. Growth Des.* **2017**, *17*, 1460−1464.
(67) Seitz, G.; Penin, N.; Decoux, L.; Wattiaux, A.; Duttine, M.; Gaudon, M. Near the Ferric Pseudobrookite Composition ($Fe_2TiO_5$). *Inorg. Chem.* **2016**, *55*, 2499−2507.
(68) Murugesan, S.; Thirumurugesan, R.; Mohandas, E.; Parameswaran, P. X-Ray Diffraction Rietveld Analysis and Bond Valence Analysis of Nano Titania Containing Oxygen Vacancies Synthesized via Sol-Gel Route. *Mater. Chem. Phys.* **2019**, *225*, 320−330.
(69) Bokhimi, X.; Pedraza, F. Characterization of Brookite and a New Corundum-like Titania Phase Synthesized under Hydrothermal Conditions. *J. Solid State Chem.* **2004**, *177*, 2456−2463.
(70) Rezaee, M.; Khoie, S. M. M.; Liu, K. H. The Role of Brookite in Mechanical Activation of Anatase-to-Rutile Transformation of Nanocrystalline $TiO_2$: An XRD and Raman Spectroscopy Investigation. *CrystEngComm* **2011**, *13*, 5055−5061.
(71) Glover, E. N. K.; Ellington, S. G.; Sankar, G.; Palgrave, R. G. The Nature and Effects of Rhodium and Antimony Dopants on the Electronic Structure of $TiO_2$: Towards Design of Z-Scheme Photocatalysts. *J. Mater. Chem. A* **2016**, *4*, 6946−6954.
(72) Quiroz, H. P.; Quintero, F.; Arias, P. J.; Dussan, A.; Zea, H. R. Effect of Fluoride and Water Content on the Growth of $TiO_2$ Nanotubes Synthesized via Ethylene Glycol with Voltage Changes during Anodizing Process. *J. Phys.: Conf. Ser.* **2015**, *614*, No. 012001.
(73) Yang, G.-J.; Li, C.-J.; Han, F.; Huang, X.-C. Effects of Annealing Treatment on Microstructure and Photocatalytic Performance of Nanostructured $TiO_2$ Coatings through Flame Spraying with Liquid Feedstocks. *J. Vac. Sci. Technol., B: Microelectron. Nanometer Struct.-Process., Meas., Phenom.* **2004**, *22*, 2364−2368.
(74) Silva Junior, E.; Porta, F. A. L.; Liu, M. S.; Andrés, J.; Varela, J. A.; Longo, E. A Relationship between Structural and Electronic Order−Disorder Effects and Optical Properties in Crystalline $TiO_2$ Nanomaterials. *Dalton Trans.* **2015**, *44*, 3159−3175.
(75) Nishio-Hamane, D.; Zhang, M.; Yagi, T.; Ma, Y. High-Pressure and High-Temperature Phase Transitions in $FeTiO_3$ and a New Dense $FeTi_3O_7$ Structure. *Am. Mineral.* **2012**, *97*, 568−572.
(76) Jain, A.; Ong, S. P.; Hautier, G.; Chen, W.; Richards, W. D.; Dacek, S.; Cholia, S.; Gunter, D.; Skinner, D.; Ceder, G.; Persson, K. A. Commentary: The Materials Project: A Materials Genome Approach to Accelerating Materials Innovation. *APL Mater.* **2013**, *1*, No. 011002.
(77) *mp-1102591: TiO2 (Cubic, Pa-3, 205)*. Materials Project. https://materialsproject.org/materials/mp-1102591/ (accessed Oct 21, 2022).
(78) *mp-1008677: TiO2 (Cubic, Fm-3m, 225)*. Materials Project. https://materialsproject.org/materials/mp-1008677/ (accessed Oct 21, 2022).
(79) Born, M. On the Stability of Crystal Lattices I. *Math. Proc. Cambridge Philos. Soc.* **1940**, *36*, 160−172.
(80) Born, M.; Huang, K.; Born, M.; Huang, K. *Dynamical Theory of Crystal Lattices*; Oxford Classic Texts in the Physical Sciences; Oxford University Press: Oxford, New York, 1998.
(81) Traylor, J. G.; Smith, H. G.; Nicklow, R. M.; Wilkinson, M. K. Lattice Dynamics of Rutile. *Phys. Rev. B* **1971**, *3*, 3457−3472.
(82) Arsov, L.; Kormann, C.; Plieth, W. Electrochemical Synthesis and in Situ Raman Spectroscopy of Thin Films of Titanium Dioxide. *J. Raman Spectrosc.* **1991**, *22*, 573−575.
(83) Ma, H. L.; Yang, J. Y.; Dai, Y.; Zhang, Y. B.; Lu, B.; Ma, G. H. Raman Study of Phase Transformation of $TiO_2$ Rutile Single Crystal Irradiated by Infrared Femtosecond Laser. *Appl. Surf. Sci.* **2007**, *253*, 7497−7500.
(84) Tompsett, G. A.; Bowmaker, G. A.; Cooney, R. P.; Metson, J. B.; Rodgers, K. A.; Seakins, J. M. The Raman Spectrum of Brookite, $TiO_2$ (Pbca, Z = 8). *J. Raman Spectrosc.* **1995**, *26*, 57−62.
(85) Gervais, F.; Piriou, B. Anharmonicity in Several-Polar-Mode Crystals: Adjusting Phonon Self-Energy of LO and TO Modes in $Al_2O_3$ and $TiO_2$ to Fit Infrared Reflectivity. *J. Phys. C: Solid State Phys.* **1974**, *7*, 2374.
(86) Eagles, D. M. Polar Modes of Lattice Vibration and Polaron Coupling Constants in Rutile ($TiO_2$). *J. Phys. Chem. Solids* **1964**, *25*, 1243−1251.
(87) Montanari, B.; Harrison, N. M. Pressure-Induced Instabilities in Bulk $TiO_2$ Rutile. *J. Phys.: Condens. Matter* **2004**, *16*, 273.
(88) Montanari, B.; Harrison, N. M. Lattice Dynamics of $TiO_2$ Rutile: Influence of Gradient Corrections in Density Functional Calculations. *Chem. Phys. Lett.* **2002**, *364*, 528−534.
(89) Mitev, P. D.; Hermansson, K.; Montanari, B.; Refson, K. Soft Modes in Strained and Unstrained Rutile $TiO_2$. *Phys. Rev. B* **2010**, *81*, No. 134303.
(90) Mikami, M.; Nakamura, S.; Kitao, O.; Arakawa, H. Lattice Dynamics and Dielectric Properties of $TiO_2$ Anatase: A First-Principles Study. *Phys. Rev. B* **2002**, *66*, No. 155213.
(91) Balachandran, U.; Eror, N. G. Raman Spectra of Titanium Dioxide. *J. Solid State Chem.* **1982**, *42*, 276−282.
(92) Gonzalez, R. J.; Zallen, R.; Berger, H. Infrared Reflectivity and Lattice Fundamentals in Anatase $TiO_2$s. *Phys. Rev. B* **1997**, *55*, 7014−7017.
(93) Beattie, I. R.; Gilson, T. R.; Anderson, J. S. Single Crystal Laser Raman Spectroscopy. *Proc. R. Soc. A* **1968**, *307*, 407−429.


https://doi.org/10.1021/acsomega.3c02038
*ACS Omega* 2023, 8, 22003−22017

(94) Iliev, M. N.; Hadjiev, V. G.; Litvinchuk, A. P. Raman and Infrared Spectra of Brookite (TiO2): Experiment and Theory. *Vib. Spectrosc.* **2013**, *64*, 148−152.
(95) Landmann, M.; Rauls, E.; Schmidt, W. G. The Electronic Structure and Optical Response of Rutile, Anatase and Brookite TiO2. *J. Phys.: Condens. Matter* **2012**, *24*, No. 195503.
(96) Zhao, X.; Vanderbilt, D. First-Principles Study of Structural, Vibrational, and Lattice Dielectric Properties of Hafnium Oxide. *Phys. Rev. B* **2002**, *65*, No. 233106.
(97) Berberich, L. J.; Bell, M. E. The Dielectric Properties of the Rutile Form of TiO $_2$. *J. Appl. Phys.* **1940**, *11*, 681−692.
(98) Hu, W.; Li, L.; Li, G.; Tang, C.; Sun, L. High-Quality Brookite $TiO_2$ Flowers: Synthesis, Characterization, and Dielectric Performance. *Cryst. Growth Des.* **2009**, *9*, 3676−3682.
(99) De Lile, J. R.; Kang, S. G.; Son, Y.-A.; Lee, S. G. Investigating Polaron Formation in Anatase and Brookite $TiO_2$ by Density Functional Theory with Hybrid-Functional and DFT+U Methods. *ACS Omega* **2019**, *4*, 8056−8064.
(100) Shibuya, T.; Yasuoka, K.; Mirbt, S.; Sanyal, B. A Systematic Study of Polarons Due to Oxygen Vacancy Formation at the Rutile $TiO_2$(110) Surface by GGA+U and HSE06 Methods. *J. Phys.: Condens. Matter* **2012**, *24*, No. 435504.
(101) Reticcioli, M.; Setvin, M.; Schmid, M.; Diebold, U.; Franchini, C. Formation and Dynamics of Small Polarons on the Rutile $TiO_2$ (110) Surface. *Phys. Rev. B* **2018**, *98*, No. 045306.
(102) Wemple, S. H. Optical Oscillator Strengths and Excitation Energies in Solids, Liquids, and Molecules. *J. Chem. Phys.* **1977**, *67*, 2151−2168.



https://doi.org/10.1021/acsomega.3c02038
*ACS Omega* 2023, 8, 22003−22017